J Mater Sci (2014) 49:7192–7212
DOI 10.1007/s10853-014-8427-5

Influence of silver nanoparticle addition, porosity, and processing technique on the mechanical properties of $Ba_{0.3}Co_4Sb_{12}$ skutterudites

Robert D. Schmidt · Eldon D. Case · Zayra Lobo · Travis R. Thompson · Jeffrey S. Sakamoto · Xiao-Yuan Zhou · Ctirad Uher

Received: 17 April 2014 / Accepted: 25 June 2014 / Published online: 15 July 2014

Abstract The thermoelectric skutterudite $Ba_{0.3}Co_4Sb_{12}$ is a promising candidate for waste heat recovery applications. Recently, it was demonstrated that the addition of silver nanoparticles (Ag_{NP}) to $Ba_{0.3}Co_4Sb_{12}$ increases both the thermoelectric figure of merit and electrical conductivity. This study is the first to examine the effect of Ag_{NP} addition on the material's mechanical properties. This study also found that the Young's modulus, E, shear modulus, G, and bulk modulus, B, decreased linearly with increasing volume fraction porosity, P. Resonant ultrasound spectroscopy was employed to measure the elastic moduli, and Vickers indentation was used to determine the hardness, H, and fracture toughness, K_C. Trends in the mechanical properties as a function of grain size, porosity, and the Ag_{NP} are discussed in terms of the pertinent literature. While K_C was independent of Ag_{NP} addition, porosity, and grain size, both E and H decreased linearly with increasing porosity. In addition, this study is the first to identify (i) the Ag_3Sb phase formed and (ii) the enhanced densification that occurs when the Ag_{NP} is sintered with $Ba_{0.3}Co_4Sb_{12}$ powders, where both effects are consistent with the eutectic and peritectic reactions observed in the binary phase diagram Ag–Sb. These eutectic/peritectic reactions may also be linked to the enhancement of electrical conductivity previously observed when Ag is added to $Ba_{0.3}Co_4Sb_{12}$. Also, similar beneficial eutectic/peritectic reactions may be available for other systems where conductive particles are added to other antimonides or other thermoelectric systems.

R. D. Schmidt · E. D. Case · Z. Lobo · T. R. Thompson · J. S. Sakamoto
Chemical Engineering and Materials Science Engineering Department, Michigan State University, East Lansing, MI, USA
e-mail: schmi402@egr.msu.edu

Z. Lobo
e-mail: zayralobo@sfhs.com

T. R. Thompson
e-mail: trthompson378@gmail.com

J. S. Sakamoto
e-mail: jsakamot@egr.msu.edu

E. D. Case (✉)
428 S. Shaw Lane, Room 3522, East Lansing, MI, USA
e-mail: casee@egr.msu.edu

X.-Y. Zhou · C. Uher
Materials Science Engineering, University of Michigan, Ann Arbor, MI, USA
e-mail: apyuanyuan@gmail.com

C. Uher
e-mail: cuher@umich.edu

Introduction

The conversion of waste heat to electrical energy by thermoelectric (TE) materials is typically characterized by the material's figure of merit, ZT, such that

$$ZT = \frac{S^2\sigma}{\kappa}T, \quad (1)$$

where S is the Seebeck coefficient, σ is the electrical conductivity, κ is the thermal conductivity, and T is temperature [1]. ZT values of up to 1.7 [2] have been reported for bulk skutterudite TE materials.

In-service conditions subject thermoelectric materials to stresses from thermal gradients, thermal transients, thermal expansion mismatch, and applied external stresses. Due to these challenges, the mechanical properties of thermoelectric materials are important, especially in waste heat harvesting applications. The response of a material to imposed

stresses requires knowledge of the elastic properties; for example, the Young's modulus and Poisson's ratio are needed in order to construct the stiffness matrix for finite element analysis [3–5]. Also, the fracture toughness, K_C, which measures the resistance to crack growth [6], is important to the mechanical integrity. In addition, hardness is related to wear characteristics of the material [7].

A key motivation for this study is the recent work on $Ba_{0.3}Co_4Sb_{12}$ by Zhou et al. [8] which showed the addition of 0.5 wt % silver nanoparticles (Ag_{NP}) leads to a 30 % increase in *ZT*, which was attributed primarily to an increase in electrical conductivity. Also, while carrier concentrations remain unchanged, a modest increase in the Seebeck coefficient also was observed with the added Ag_{NP} [8].

In general, the nanostructural and microstructural details can be extremely important for the transport properties of thermoelectric materials, and many previous studies have used nanostructures to reduce thermal conductivity by enhancing phonon scattering [9–15], which can lead, in turn, to increases in *ZT*. Also, reducing the grain size or increasing porosity can enhance phonon scattering and thus increase *ZT* [16, 17].

Although in this study, an increased porosity leads to decreases in the elastic moduli, an increase in porosity also has the potential to increase the resistance to thermal fatigue damage [18, 19], which is important due to the inevitable thermal cycling that thermoelectrics are subjected to during waste heat harvesting. In addition to affecting mechanical properties, porosity also impacts transport properties. In thermoelectrics such as nanoporous GeSi alloys [20], porosity decreases both the electrical and thermal conductivity, although the decrease in electrical conductivity overwhelms the decrease in thermal conductivity, resulting in a net lowering of *ZT* due to porosity. However, in skutterudites including $La_{0.75}Fe_3CoSb_{12}$ [21], $Co_{0.9}Ni_{0.1}Sb_3$, $Co_{0.8}Ni_{0.2}Sb_3$ [22], and a TiN nanoparticles-$Co_4Sb_{11.5}Te_{0.5}$ composite [23], enhancements in *ZT* have been reported for porosity levels between $P = 0.003$ and 0.15. For example, Wen et al. [23] densified a 0.01 volume fraction TiN nanoparticles-$Co_4Sb_{11.5}Te_{0.5}$ skutterudite, and subsequent thermal annealing at 773 K for 120 h in vacuum led to bloating (the formation of internal porosity) and a 10 % increase in porosity which Wen et al. ascribed to a reaction between the TiN nanoparticles and the $Co_4Sb_{11.5}Te_{0.5}$ matrix phases. Wen et al. noted that "The electrical conductivity and the thermal conductivity of the annealed sample decline simultaneously due to the higher porosity, but the thermal conductivity reduces more remarkably", leading to a 20 % increase in *ZT* compared to the denser specimens (prior to annealing and bloating) [23]. Thus, in addition to having the potential to boost thermal fatigue resistance, in some skutterudites, porosity can increase *ZT* making it important to also assess the mechanical properties such as elastic moduli, hardness, and toughness for porous thermoelectrics.

In this study, we examine the Young's modulus, *E*, shear modulus, *G*, bulk modulus, *B*, Poisson's ratio, *v*, hardness, *H*, and fracture toughness, K_C, of $Ba_{0.3}Co_4Sb_{12}$ with and without the addition 0.5 wt % Ag_{NP}. We further explore the effects of microstructure/nanostructure and processing pursuing two processing routes: (i) planetary milling (PM), then hot press (HP) sintering and (ii) vibratory milling (VM) followed by pulsed electric current sintering (PECS). In this way, we produced specimens with a range of porosity and grain size while using the two most common milling techniques (planetary milling and vibratory milling) and densification techniques (HP and PECS) used to process thermoelectric materials.

Experimental procedure

Materials and specimen preparation

To fabricate $Ba_{0.3}Co_4Sb_{12}$, elemental Ba (pieces, 99.9 % pure), Co (powder 99.5 % pure), and Sb (shot 99.999 % pure) in stoichiometric ratio were placed inside evacuated carbon coated quartz ampoules, heated to 1100 °C and held at that temperature 5 h, then quenched into a supersaturated salt water solution. The resulting ingots were then annealed at 750 °C for 7 days. Finally, the ingots were planetary ball milled.

In this study, two different processing techniques were used to fabricate two sets of specimens with differing microstructures. First, Ag_{NP} powders, which had a vendor-specified purity of 99.9 % and a size range of from 20 to 40 nm (45509, Alfa Aesar, Ward Hill MA), were dispersed into the $Ba_{0.3}Co_4Sb_{12}$ powder by planetary ball milling at 300 rpm for 15 min [24]. Then specimens approximately 10.5 mm in diameter and 10 mm in height were fabricated by hot pressing $Ba_{0.3}Co_4Sb_{12}$ powders (with and without the added Ag_{NP}) in a graphite die for 20 min in an argon atmosphere with 50 MPa pressure at temperatures of 673, 773, or 873 K in order to produce specimens with a range of volume fraction porosity, *P*, from 0.30 to 0.05 (Table 1). The hot-pressed specimens were then cut into disks approximately 1.7-mm thick using a slow speed saw (Isomet, Buehler, Lake Bluff IL) with 0.3-mm-thick diamond blade (801-137, Leco Corp., St. Joseph, MI).

A second set of specimens was fabricated by reprocessing the specimens hot pressed without Ag_{NP} additions by first grinding the hot-pressed specimens without Ag addition in an automated mortar and pestle (PM100, Retch) and then sieving with a 75-μm sieve, where the grinding and sieving steps were performed in an argon-filled glove box containing less than 10 ppm oxygen. Using Viton gaskets (WC mill

Table 1 Specimens of skutterudite $Ba_{0.3}Co_4Sb_{12}$ used in this study varied based on Ag_{NP} addition, sintering procedure and temperature, resulting porosity, and powder processing

Specimen	Ag_{NP} addition	Powder processing	Sintering procedure	Sintering temperature (K)	Vol. fraction porosity
PM-HP-673	No	PM	HP	673	0.30
PM-HP-773	No	PM	HP	773	0.21
PM-HP-873	No	PM	HP	873	0.16
PM-HP-673-Ag	Yes	PM	HP	673	0.27
PM-HP-773-Ag	Yes	PM	HP	773	0.18
PM-HP-873-Ag	Yes	PM	HP	873	0.05
VM-PECS-673	No	VM	PECS	673	0.16
VM-PECS-723	No	VM	PECS	723	0.13
VM-PECS-773	No	VM	PECS	773	0.09

Specimens VM-PECS-673, VM-PECS-723 and VM-PECS-773 were reprocessed from specimens PM-HP-673, PM-HP-773 and PM-HP-873 by grinding and powder processing by vibratory milling, and sintering by PECS

PM planetary milling, *VM* vibratory milling, *HP* hot pressed, *PECS* pulsed electric current sintering

jar set 8004, WC media 5004A, Viton gasket 39322, SPEX Sample Prep, Metuchen, NJ), the resulting 7.1 g ground powder batches were sealed in a WC mill jar with a total of six spherical WC milling media (two WC spheres 11.2 mm in diameter and four WC spheres 7.9 mm in diameter). In order to perform vibratory milling outside the glove box, prior to removing the mill jar from the glove box, the mill jar and end cap were wrapped with electrical tape (Super 88, 3 m, St. Paul, MN) and Parafilm "M" (PM-996 Pechiney Plastic Packaging, Menasha WI). The powders were milled for 10 min in a vibratory mill (8000 M SPEX SamplePrep) then the mill jar was returned to the glove box. The reading of the oxygen meter on the glove box did not change when the mill jar was opened in the glove box. The oxygen meter is sensitive to changes within ±0.1 ppm, implying that the sealing of the mill jar was effective. The vibratory milled powder then was sintered in an argon atmosphere by PECS (SPS Model 10-3, Thermal Technology LLC, Santa Rosa, CA) in a grafoil-lined graphite die at 673, 723, or 773 K for 10 min with 50 MPa pressure (Table 1), producing disk-shaped specimens approximately 12.6 mm in diameter and 2.6-mm thick.

Elasticity measurements

Resonant ultrasound spectroscopy (RUS) elasticity measurements were performed using a tripod arrangement of piezoelectric transducers. A driving transducer which was swept through a range of frequency from 35 to 485 kHz excited mechanical resonances in the specimen which were detected via the two pickup transducers. The peaks in the intensity versus frequency output of the pickup transducers (Fig. 1) represent the mechanical resonance frequencies of the specimen. From the resonant frequencies, specimen mass, dimensions, and geometry, the elastic moduli of the

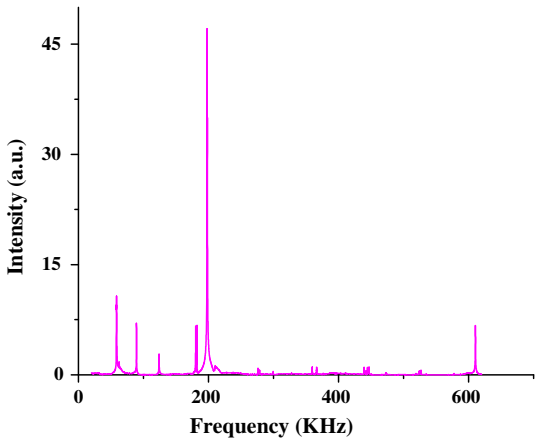

Fig. 1 RUS spectrum from specimen PM-HP-873-Ag, $P = 0.05$ with Ag_{NP}. The elastic moduli of each of the specimens in this study are calculated from the specimen mass, dimensions, shape, and resonant frequencies. *Each peak* in the spectrum represents a mechanical resonance at that frequency

disk-spaced specimens were calculated using commercial software (RUSpec and CylModel, Quasar International, Inc., Albuquerque, NM). Additional details of the RUS procedure are provided elsewhere [25–29].

Hardness and toughness measurements

Prior to indentation measurements of H and K_C, and prior to energy-dispersive X-ray spectroscopy measurements, the specimens were polished with diamond paste with grit sizes ranging from 30–1 μm. At least ten indentations per load for loads of 1.96, 2.94, 4.9, and 9.8 N were made on the polished surface of each specimen, with a loading time of 5 s for each indentation. Prior to the hardness measurements, the Vickers indenter was calibrated using a steel

standard calibration block (Yamamoto Scientific Tools Lab Co. LTD, Chiba, Japan). The hardness calibration factor, ζ, ranged from 0.95 to 0.97 for the indentation loads used in this study. The hardness, H, for indentation was calculated from [30]

$$H = \zeta \frac{1.8544F}{(2a)^2} \quad (2)$$

where F is the applied indentation load and a is half of the diagonal length of the indentation impression.

The fracture toughness, K_C, was calculated from

$$K_C = \frac{\xi (E/H)^{0.5} F}{c^{3/2}} \quad (3)$$

where ξ is a dimensionless calibration constant equal to 0.016 [6], E is the Young's modulus measured by RUS, H is the hardness value and c is half of the radial crack length and F is the applied load [6].

Energy-dispersive X-ray spectroscopy and microscopy

Except for specimen PM-HP-673-Ag, each of the sintered specimens was first polished and then examined by energy-dispersive X-ray spectroscopy (EDS). However, polishing was unsuccessful for PM-HP-673-Ag, so the examined surfaces were those cut by a low speed diamond saw.

The microstructure and nanostructure of the powders and sintered specimens were observed by scanning electron microscope (SEM, JEOL 6610LV or JSM-7500F, JEOL Ltd., Japan) at a 15 kV accelerating voltage and either a 15 or 8 mm working distance. Using SEM micrographs of the fracture surfaces of sintered specimens, the grain size of sintered specimens was determined using the linear intercept method with at least 200 intercepts per micrograph and a stereographic projection factor of 1.5 [31, 32]. The microstructure of the polished specimen surfaces was observed using the secondary electron image (SEI) mode. Atomic number contrast was observed in the backscattered electron image (BEI) mode. Compositions were determined in the BEI mode using EDS. For SEM observation, all specimens were mounted on aluminum stubs, where the silver nanoparticles were adhered to the stubs using carbon paint (05006-AB, SPI Supplies, West Chester, PA), and the sintered specimens were mounted using carbon tape.

Results and discussion

Microstructural and chemical analysis

The addition of Ag_{NP} resulted in a greater change in density at the higher sintering temperature than the specimen without Ag_{NP} addition (Table 1). When HP sintered at 673 K, the porosity was nearly identical for the specimen without ($P = 0.30$) and with Ag_{NP} ($P = 0.27$), but when sintered at 873 K, the specimen without Ag_{NP} addition ($P = 0.16$) was significantly less dense than the specimen with Ag_{NP} addition ($P = 0.05$). The density difference for specimens sintered at the same temperature requires a close examination of the microstructural features of the Ag_{NP} addition, examined in two parts.

The microstructural and nanostructural features examined in this study included (i) the as-received Ag_{NP} powders (Fig. 2), and for the sintered $Ba_{0.3}Co_4Sb_{12}$ specimens the micron-sized Ag inclusions (Figs. 3, 4) in "Microstructure of the AgNP and Ag agglomerates" section, and (ii) porosity (Figs. 5, 6, and 7) as well as grain size and size distribution (Figs. 5, 6, 8) in "Porosity and grain size and relationship to the processing technique" section.

Microstructure of the Ag_{NP} and Ag agglomerates

The as-received Ag_{NP} powders consisted of (i) large, irregularly shaped agglomerates up to 30 μm across, with most agglomerates being between 0.5 and 10 μm in diameter, (ii) individual spherical nanoparticles with diameters 30 nm (Fig. 2d) and (iii) small clusters of nanoparticles (Fig. 2). Similar agglomerates, small clusters, and individual Ag_{NP} are visible in micrographs taken by Zhou (Fig. 2a of Zhou 2012]) of Ag_{NP} powders received from the same vendor as in this study.

After hot pressing at 673, 773, and 873 K, the consolidated, micron-size Ag particles observed in the $Ba_{0.3}Co_4Sb_{12}$ specimens with 0.5 wt % Ag_{NP} (Figs. 3, 4) had roughly the same dimensions as the original Ag_{NP} agglomerates present in the as-received Ag_{NP} powders (Fig. 2). In the sintered specimens, the typical dimension of Ag particles observed in PM-HP-773-Ag and PM-HP-873-Ag was between 0.3 and 10 μm, with a few Ag particles of 20-μm diameter or greater, as observed by backscatter electron images of polished surfaces (Figs. 3, 4). Thus, the Ag_{NP} agglomerates may not have broken up significantly during mixing in the planetary mill prior to hot pressing.

As a rough gauge of how easily the Ag_{NP} agglomerates can be broken apart by milling, 0.0225 g of Ag_{NP} was wet milled by hand for 60 s in a porcelain mortar and pestle (60310 and 60311, CoorsTek, Golden, CO) with 5 mL of ethanol. After milling, the Ag_{NP} agglomerates were still present but some surfaces of the agglomerate surfaces appeared to be deformed by the hand milling and some of the nanoparticles on the deformed surfaces of the agglomerates appeared to be smeared (Fig. 9). After hand milling, the Ag_{NP} agglomerates typically ranged in diameter from sub-micron to 100 μm (Fig. 9), similar to or greater than the dimensions of Ag_{NP} agglomerates before milling. Thus, based on both the SEM examination of the

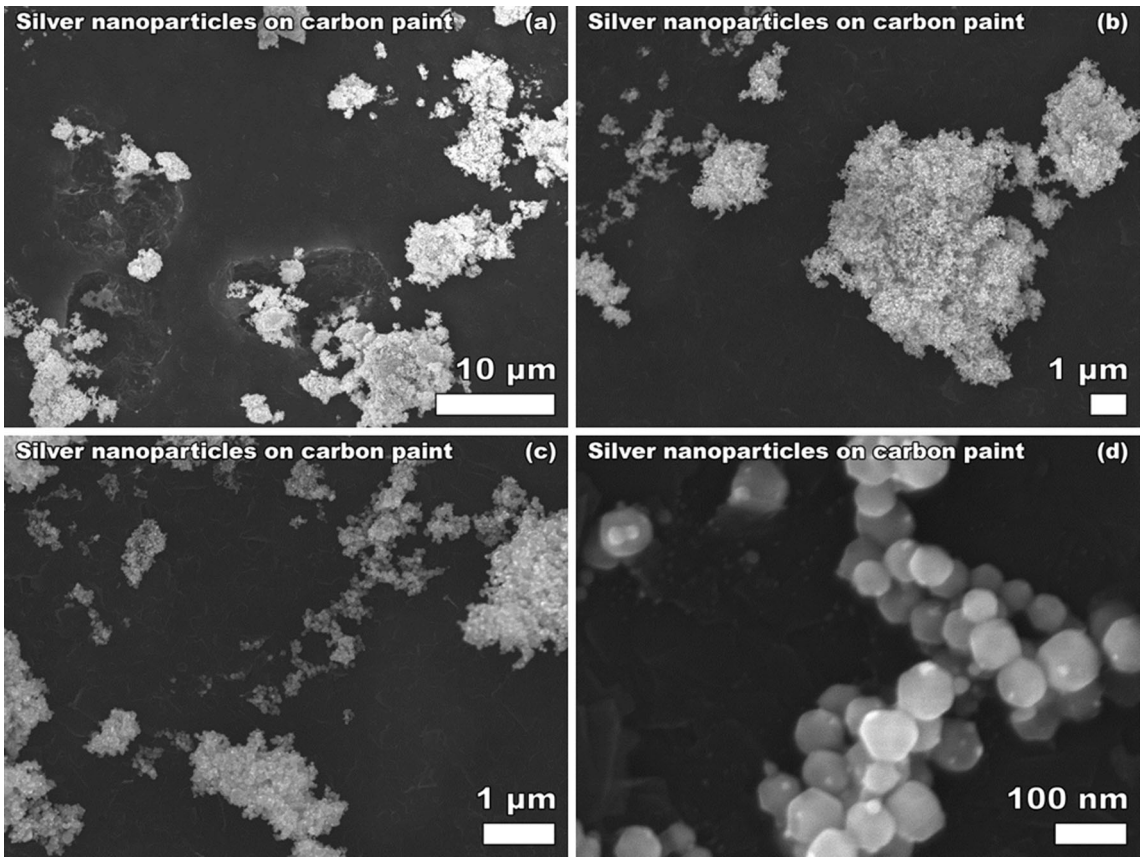

Fig. 2 Silver nanoparticles exhibited agglomerates of 10 μm or greater (**a**–**c**), but consisting of individual grains or particles consistent with the manufacturer claimed average particle size of 20–40 nm (**d**)

Ag_{NP} agglomerates before and after hand milling, the hand milling process did not appear to significantly break up the agglomerates.

While the hand milling conditions are likely different than those encountered during the planetary milling, it is likely that some of the original Ag_{NP} agglomerates in the as-received powders survived (at least partially intact) the mixing process with the Ag_{NP} agglomerates powders to give the micron-sized consolidated Ag particles observed in the as-sintered Ba-skuttterudite-Ag_{NP} specimens in this study. This is further supported by the SEM-based observation that the size of the Ag_{NP} agglomerates in the powders is similar to the size of the Ag particles in the sintered specimens. Thus, it does not seem to be necessary to postulate an accretion of Ag_{NP} during milling to explain the present of micron-sized Ag particles in the sintered specimens.

Porosity and grain size and relationship to the processing technique

The six hot-pressed specimens included this study (Table 1) showed a bimodal grain size distribution (Figs. 5, 6) consisting of a polycrystalline matrix with grain sizes ranging from approximately 0.3–3 μm, with an average grain size (*GS*) of roughly 1 μm. Also, grains approximately 5–20 μm across were observed in each HP specimen, both without Ag_{NP} (Fig. 5) and with Ag_{NP} (Fig. 6) additions. Pores with diameters of submicron to a few microns across were distributed through the matrix, consisting of open, interconnected porosity when sintered at 673 K, and consisting of partially to fully isolated porosity at 773 K and 873 K (Figs. 5, 6). The observed pore morphologies for the specimens sintered at 673, 773, and 873 K agrees with the pore evolution in sintered powders [33].

Each of the three reprocessed specimens (vibratory milled and then sintered via PECS at 773, 723, and 673 K) had a much different microstructure than those obtained by planetary milling and hot pressing. Namely, the VM-PECS specimens a unimodal *GS* distribution (Fig. 8) with a significantly smaller average *GS* of 0.17, 0.14, and 0.15 μm, respectively, than the specimens that were planetary milled and hot pressed. The reprocessed specimen VM-PECS-773 had a volume fraction porosity of only 0.09, which included dense regions with clusters of pores (Fig. 7c). However, specimen VM-PECS-673 included clusters of pores with islands of denser material (Table 1; Fig. 7a). The microstructure of specimen VM-PECS-723 was intermediate in between specimens VM-PECS-773 and VM-PECS-673 (Table 1; Fig. 7b).

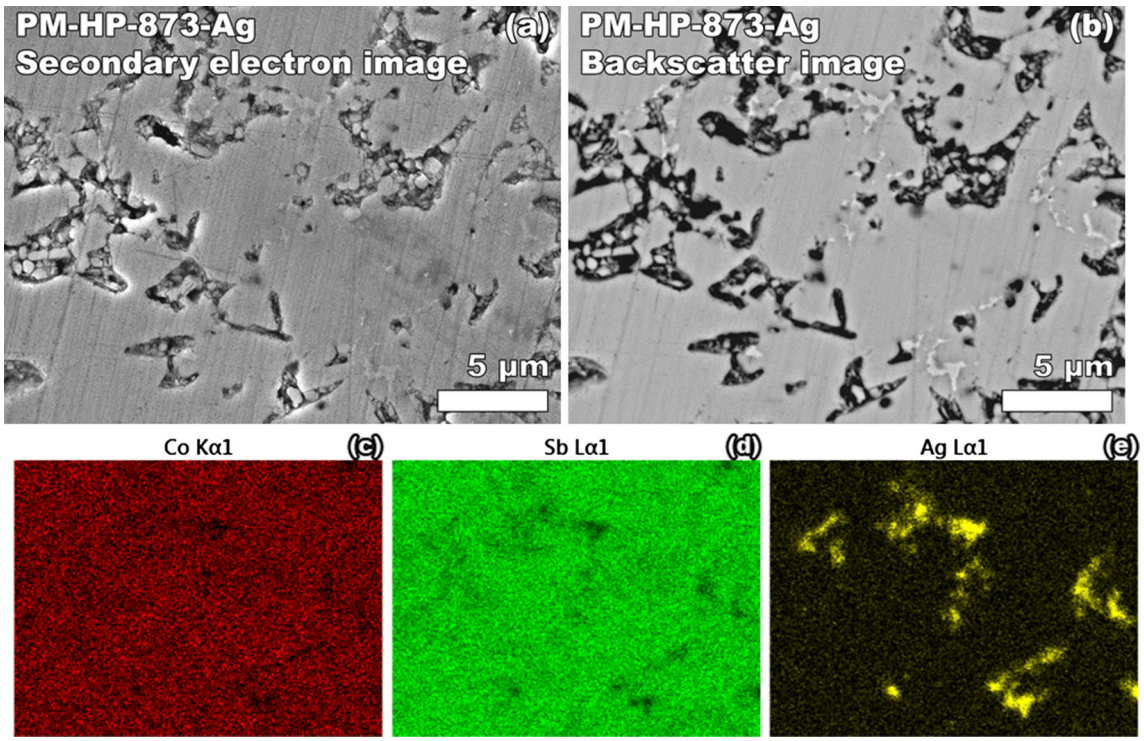

Fig. 3 Polished surfaces of specimen PM-HP-873-Ag, both in secondary electron images (**a**) and backscatter images (**b**). Porosity is observed between larger grains (**a** and **b**), but also with areas of Ag visible in backscatter as bright areas (**b**), due to the higher average atomic weight of the silver-rich regions. The abundance of Ag and the relative deficiency of Co or Sb in the bright areas of the backscatter image (**b**) is confirmed by energy-dispersive X-ray spectroscopy maps (**c–e**)

The addition of Ag_{NP} results in an increased density of hot-pressed specimens at a sintering temperature of 873 K, where the specimen without Ag_{NP} had a P value of 0.16 while the specimen sintered with 0.5 wt % Ag_{NP} had $P = 0.05$ (Table 1). At a hot press sintering temperature of 773 K, the porosities of the specimens with and without 0.5 wt % Ag_{NP} were 0.18 and 0.21, respectively (Table 1). Also, for a sintering temperature of 673 K, the porosities of the specimens with and without 0.5 wt % Ag_{NP} were 0.27 and 0.30, respectively (Table 1). Thus, hot press sintering at 773 and 673 K resulted in similar porosities for specimens with and without 0.5 wt % Ag_{NP} additions. However, the Ag_{NP} addition resulted in considerably enhanced densification for hot press sintering at 873 K. The enhanced sintering is likely related to a reaction between the 0.5 wt % Ag_{NP} addition and the $Ba_{0.3}Co_4Sb_{12}$ matrix, as discussed in "Chemical analysis" section.

Chemical analysis

Chemistry of the Ag_{NP} and Ag agglomerates

EDS analysis showed the as-received Ag_{NP} powder to be 99.5 at % Ag, with oxygen and Al impurities (Table 2). The Al in the EDS analysis likely originated from the aluminum stub on which the specimens were mounted.

Polished surfaces of specimens PM-HP-873-Ag and PM-HP-773-Ag were examined by EDS, with matrix region and Ag-rich regions in each specimen examined separately at the points indicated in Figs. 4c and e, and line scans extending across both matrix material and Ag-rich regions (Fig. 4c–f). As determined by EDS, the elemental composition of the matrix region is consistent with $Ba_{0.3}Co_4Sb_{12}$ (Tables 3, 4; Fig. 4c–f). In the Ag-rich regions, the composition is consistent with primarily Ag_3Sb phase material. In specimen PM-HP-873-Ag, the Ag:Sb ratio was 3.0:1 to 3.3:1 in the silver-rich regions (Table 3; Fig. 4e), and in specimen PM-HP-773-Ag, the ratio was 2.5:1 (Table 4; Fig. 4c). Less than 2 at % Co was detected in each of the silver-rich regions, consistent with little to no skutterudite phase present in the silver-rich regions.

In contrast to the preparation of specimens PM-HP-873-Ag and PM-HP-773-Ag, specimen PM-HP-673-Ag was cut on a low speed diamond saw because the high porosity of the specimen ($P = 0.27$, Table 1) made it too friable for polishing. The elemental composition of the matrix region is consistent with $Ba_{0.3}Co_4Sb_{12}$ (Table 5; Fig. 4a, b). In the Ag-rich regions of PM-HP-673-Ag, the Ag:Sb ratio was

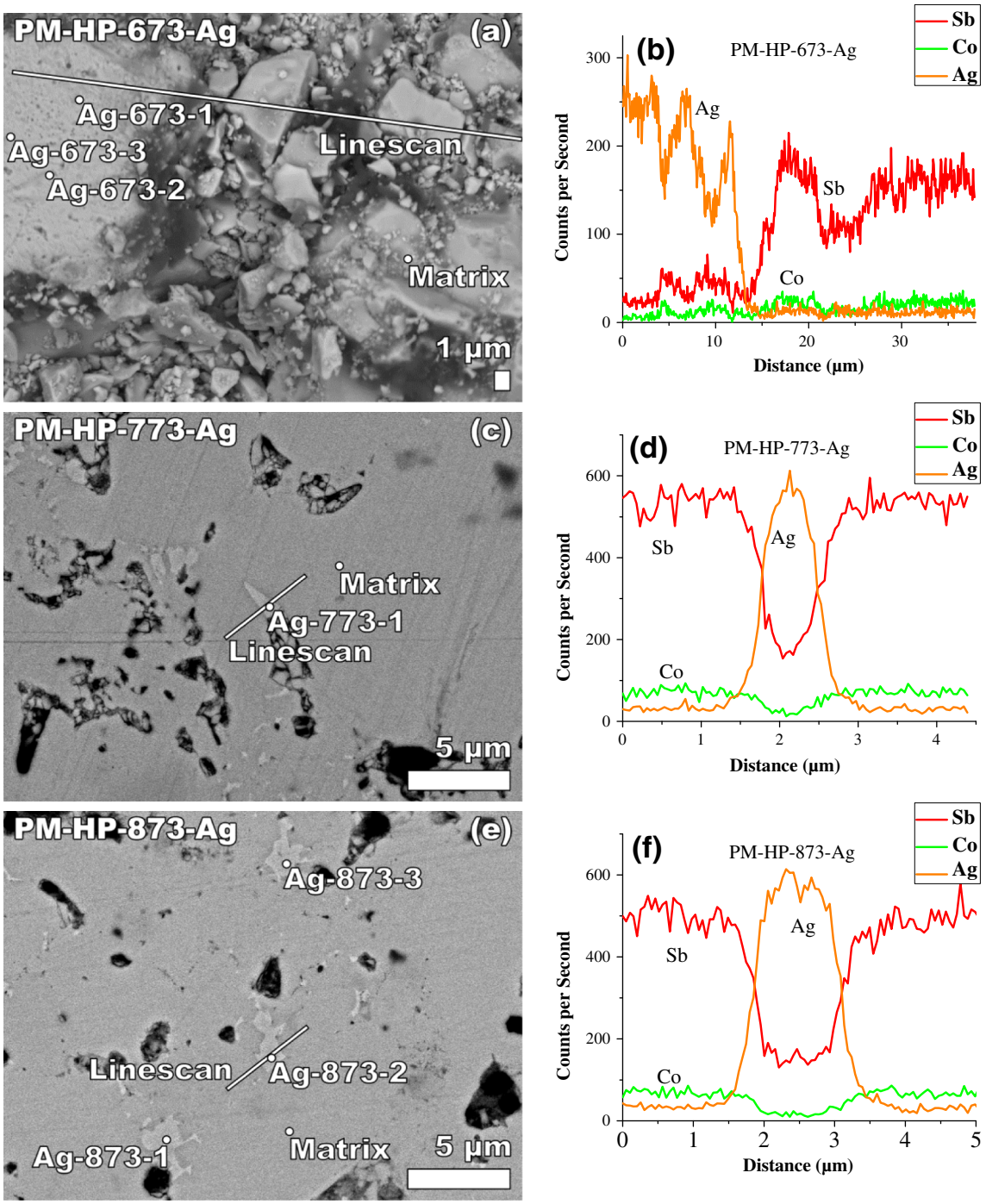

Fig. 4 For each of the hot pressed specimens with Ag_{NP} additions, an EDS line scan was performed and point ID locations were chosen. For PM-HP-673-Ag, a cut surface was used (**a**) because the specimen was not successfully polished. For PM-HP-773-Ag and PM-HP-873-Ag, polished surfaces were examined (**c** and **e**). The line scan for PM-HP-673-Ag (**b**) indicated only silver present except for two regions in the silver where antimony and cobalt were present in concentrations consistent with skutterudite particles. In contrast, the line scan for PM-HP-773-Ag (**d**) and PM-HP-873-Ag (**f**) indicated the presence of antimony in the silver-rich locations. No silver was observed in the matrix outside of the silver-rich locations

highly variable, with ratios of 3.4:1, 13.3:1, and 16.3:1 (Table 5), which is more indicative of a mixture than a single phase. In the Ag-rich location with the highest concentration of Sb, Ag-673-1, a significant concentration of Co was also detected, 6.80 at %, and in a Co:Sb ratio of 1:3.1 (Table 5), consistent with a particle or particles of $Ba_{0.3}CoSb_3$ (matrix material) embedded in otherwise pure Ag. Particles of $Ba_{0.3}CoSb_3$ may have become embedded

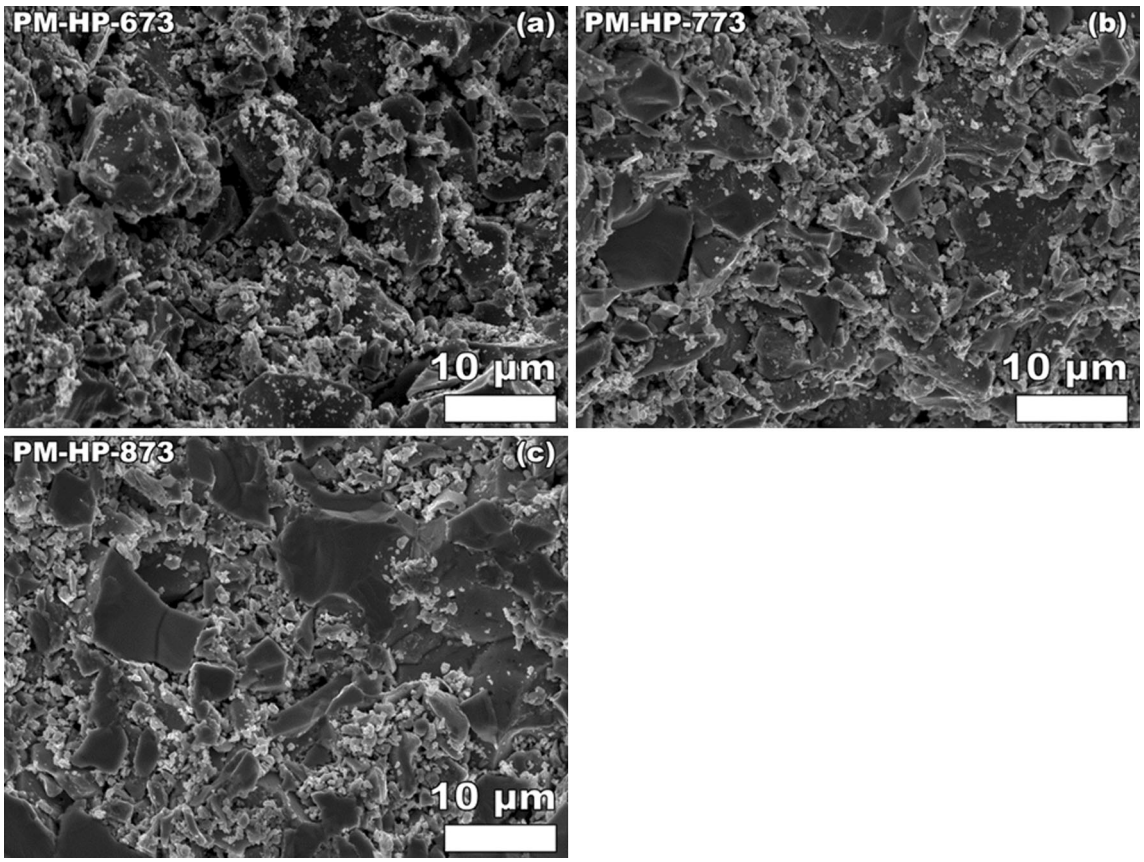

Fig. 5 The microstructure of $Ba_{0.3}Co_4Sb_{12}$, without Ag addition, changed as a function of sintering temperature. For **a** a sintering temperature of 673 K, microstructure and porosity, *P*, are consistent with a specimen with little to no observed sintering or densification. After sintering at 773 K (**b**), only minimal densification and neck formation are observed. Hot pressing at 873 K (**c**), enhanced both grain growth and densification in the specimen without Ag nanoparticles, however, the microstructure still is observed to be very porous, consistent with measurement of $P = 0.16$

in the Ag-rich region during cutting. The presence of small, discrete skutterudite particles embedded in the silver in specimen PM-HP-673-Ag is further supported by the line scan (Fig. 4b), in which there are two dips in the counts of silver at distances of 5 and 10 μm, with corresponding increases of both Co and Sb counts at each location. The EDS results from the other two Ag-rich locations, Ag-673-2 and Ag-673-3 (Table 5), are primarily pure Ag material, with no indication of embedded $Ba_{0.3}CoSb_3$ particles.

Sintering behavior changes and scavenging of Sb

Although the $Ba_{0.3}Co_4Sb_{12}$-Ag composition is within a quaternary Ba–Co–Sb–Ag system for which no phase diagram is available, the Ag–Sb binary phase diagram may provide important guidance to understanding the formation of Ag_3Sb particles. In the binary phase diagram for Ag–Sb, there are only two intermediate compounds, Ag_3Sb and Ag_6Sb [34–36]. Upon cooling, Ag_3Sb forms via a peritectic reaction $Ag_6Sb + L \Leftrightarrow Ag_3Sb$ at 835 ± 2 K and an initial Sb concentration of 21.2 at % [36]. Also, the eutectic reaction $L \Leftrightarrow Ag_3Sb + Sb$ occurs at 757 K with a eutectic composition reported as 38 at % Sb [34, 37, 38] or 41 at % Sb [39].

In the present research, the Sb that reacts with the Ag_{NP} may be scavenged from the $Ba_{0.3}Co_4Sb_{12}$ matrix. Scavenging of excess Sb can aid thermal stability in skutterudites. For example, Zhang and Sakamoto found that the Sb deficient specimens of $Fe_{3.5}Co_{0.5}Sb_{12}$-based skutterudites were more dimensionally stable than specimens with excess Sb [40].

The presence of a transient liquid phase is known to greatly enhance densification during sintering [33], thus the enhanced densification for the Ba–skutterudite–Ag_{NP} specimens observed in this study ("Microstructural and chemical analysis" section, Table 1) may be due to a transient liquid phase during sintering associated with the peritectic and eutectic reactions in the Ag–Sb system. Also, if the liquid phase wets the grain boundaries, the electrical conductivity of the grain boundaries could be greatly enhanced, by a surface film rather than only point contacts due to discrete Ag_{NP} or Ag particles, as was suggested by Zhao et al. [8]. A similar binary and ternary eutectic in

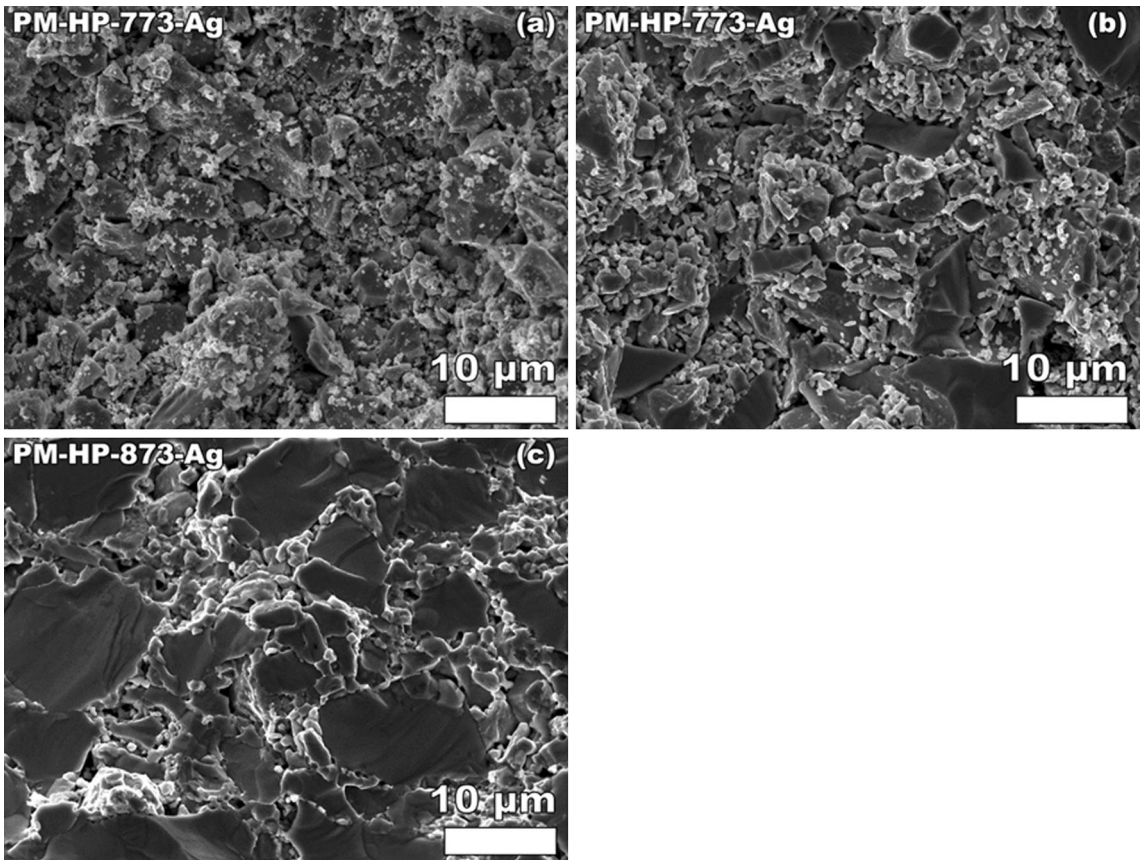

Fig. 6 The microstructure of $Ba_{0.3}Co_4Sb_{12}$ with 0.5 wt % Ag_{NP} addition changed as a function of sintering temperature. At 673 K (**a**), little to no sintering is observed in the microstructure. Hot pressing at 773 K (**b**) resulted in limited grain growth and densification, with necks observed between the grains but significant porosity observed, consistent with early stage sintering. The porosity for the specimen with Ag nanoparticles sintered at 873 K (**c**) is the lowest ($P = 0.03$) of all the specimens in this study

lead-free Sn–Ag–Cu solders aids in wetting the surfaces of electrical wires, pins, or pads [41, 42].

Possible significance to other thermoelectric material systems

The proposed reaction of Ag with Sb in Ba-filled skutterudite $Ba_{0.3}Co_4Sb_{12}$ has important implications for other skutterudites, other antimonides, and even other thermoelectric systems. In this study, the Ba-filled skutterudite is $CoSb_3$-based, but more generally unfilled skutterudites have the general composition TX_3, where T is a transition metal element (Co, Fe, Ni) and X is a pnicogen element (Sb, As, and P) [43]. "Filler" atoms, often a rare earth element or mischmetal added to the skutterudite composition, scatter phonons to make them an important class of thermoelectric materials [44–48]. Many $CoSb_3$-based and $FeSb_3$-based compositions have been studied in the literature [49], so in addition to the particular Ba-filled skutterudite included in this study, adding Ag_{NP} to other antimonide skutterudites may well lead to the same type of Ag–Sb reaction and thus liquid phase sintering, the formation of Ag_3Sb, enhanced densification and improvements in the *ZT* and electrical conductivity. Also, for an antimonide thermoelectric that is not a skutterudite, a recent study by Xiong [50] shows that Ag added to ZnSb leads to the formation of Ag_3Sb particles and a higher electrical conductivity.

This type of reaction may not be limited to Ag and antimonides. In fact, there may be other conductive metal-thermoelectric material combinations in which similar peritectic/eutectic reactions occur, accompanied by similar beneficial effects. One guide to searching for such systems would be appropriate binary or ternary phase diagrams.

Elasticity results

The measured elastic moduli are essentially independent of the Ag_{NP} addition and the processing/grain size, but are strong functions of porosity (Fig. 10a–c).

Elasticity as a function of Ag_{NP} addition

In order to determine whether or not the elastic moduli are functions of the Ag_{NP} addition, for the set of specimens (with

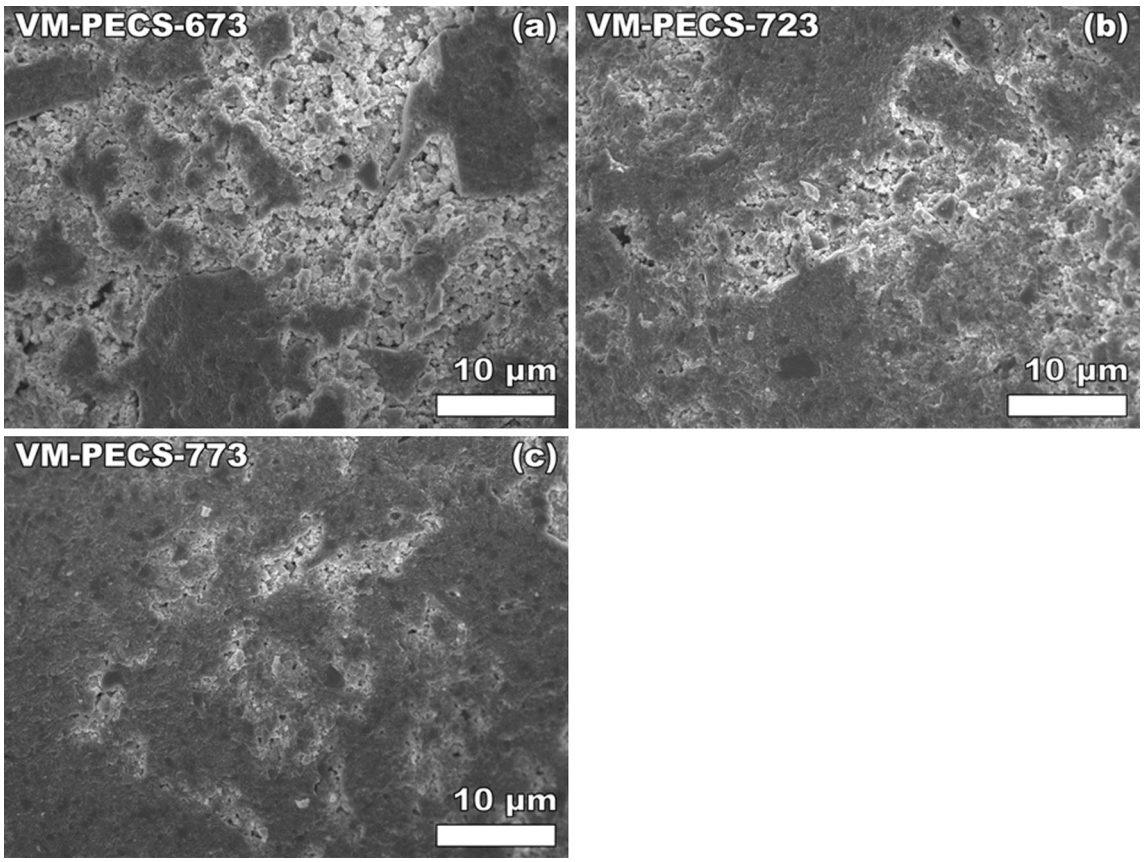

Fig. 7 Fracture surface images of reprocessed material sintered by PECS exhibit dense regions surrounded by regions of higher porosity. All regions of the specimens exhibit similar grain sizes. The porous areas decrease as the sintering temperature increased from **a** 673 K, to **b** 723 K, to 773 K

and without Ag_{NP} addition) included in this study, we examined the porosity dependence of Young's modulus, shear modulus, and bulk modulus (Table 1; Fig. 10). There are no significant differences between the slope and intercept for the least-squares fit to the data (i) with and (ii) without Ag_{NP} additions, with coefficient of determination, R^2, values of 0.955 to 0.998 for E and G, and R^2 of 0.857 and 0.947 for B (Fig. 10).

To put the elasticity dependence on Ag_{NP} addition into context, the literature shows that the elastic modulus as a function of the overall composition depends on the physical nature of the material system itself, where compositional changes can occur when one has (i) a composite system in which discrete particles are added to a matrix of differing composition or (ii) a solid solution system or (iii) a solid solution system that includes micro- or nano-scale particles. Changes in elastic moduli of a particulate composite as a function of the addition of a given volume percent of particulate phase have been modeled by a number of researchers [51–54] (Appendix). The four composite models given in Appendix predict a decrease in the elastic modulus of the composite, E_C of about 0.39 % with the 0.5 wt % Ag_{NP} addition to the Ba-skutterudite in this study.

Elastic moduli and porosity

The elastic moduli of the skutterudite $Ba_{0.3}Co_4Sb_{12}$ in this study are linear functions of porosity over the range of volume fraction porosity included in this study (between 0.05 and 0.30, Table 6; Fig. 10). In addition, the elastic modulus versus porosity data is independent of either the presence or absence of the 0.5 wt % Ag_{NP} (Table 6; Fig. 10). Also, the powder processing technique (planetary milling or vibratory milling) and the densification method (hot pressing or PECS) (Table 1) do not affect the elastic modulus versus porosity behavior (Table 6; Fig. 10).

The elastic moduli of TE materials are porosity dependent [29, 55]. An empirical expression frequently used to describe the porosity dependence of Young's modulus, E, shear modulus, G, and bulk modulus, B [29, 55], of brittle materials [56], including TE materials [29, 55]

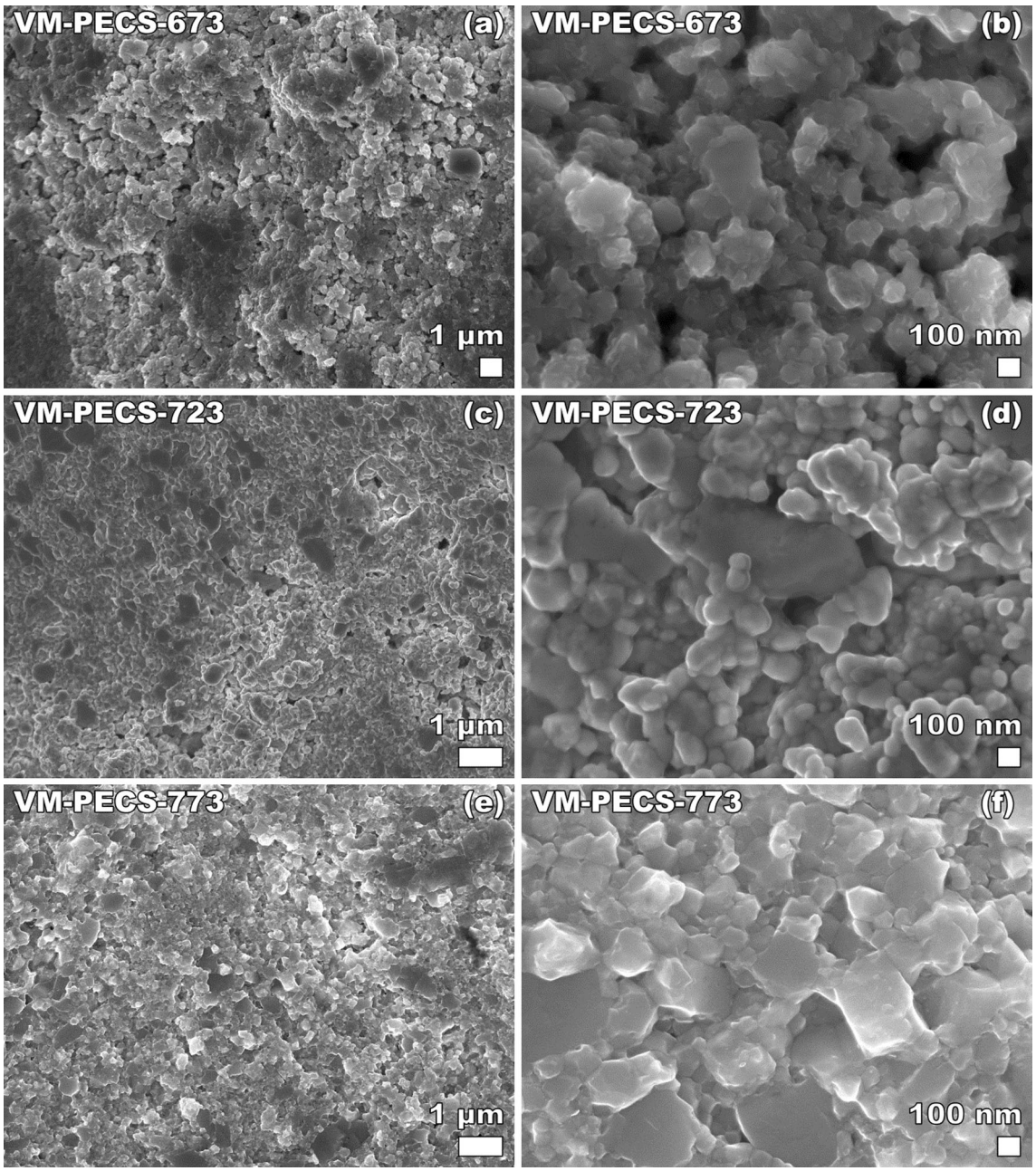

Fig. 8 After reprocessing by SPEX milling and sintering by PECS, the samples exhibit a unimodal, sub-micron grain size distribution

$$A = A_0(\exp -b_A P) \tag{4a}$$

where A represents the property E, G, or B [56] and b_A is a unitless, material-dependent parameter that measures the rate of decrease in property A with increase P. If $b_A P$ is small, the equation may be linearized by using the first two terms of the Taylor series expansion of Eq. (4a) [29].

$$A = A_0(1 - b_A P) \tag{4b}$$

For the nine $Ba_{0.3}Co_4Sb_{12}$ specimens in this study (with and without Ag_{NP} addition), a least-squares fit of the modulus data to Eq. (4b) yielded $P = 0$ intercept values of $E_0 = 145.1 \pm 5.2$ GPa, $G_0 = 59.8 \pm 2.0$ GPa, and $B_0 = 84.9 \pm 5.9$ GPa with coefficients of determination, R^2, of at least 0.90 for E, G, and B. There is no significant difference between the $P = 0$ intercept for the three specimens with 0.5 wt % Ag_{NP} as compared to the six specimens without Ag_{NP} addition (Table 6). Also, the rate of decrease in modulus with porosity (given by b_A in Eq. (4b)) was between 3.0 and 3.2 for the $Ba_{0.3}Co_4Sb_{12}$ (Table 6), which is consistent with values of 2 to 6 for a wide range of solid materials [56].

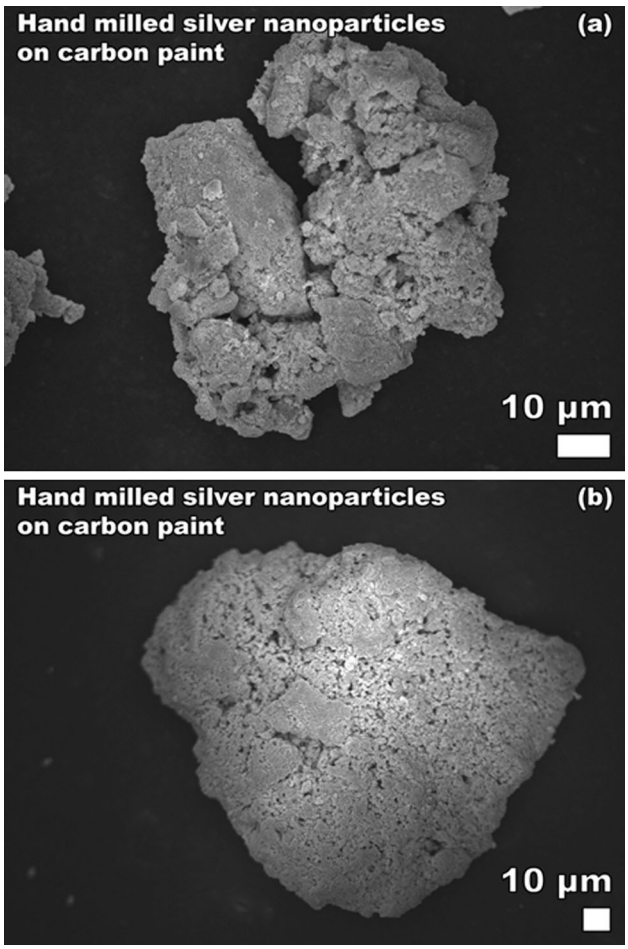

Fig. 9 Hand milling of Ag_{NP} agglomerates in ethanol were not observed to reduce the size of the nanoparticle agglomerates. After hand milling, silver nanoparticle agglomerates of 10 μm or greater were typically observed, similar to the size of agglomerates for the as-received Ag_{NP}. Several faces of the agglomerates appear to be deformed after hand milling

Table 2 Results of EDS scan using Point ID mode on two as-received Ag_{NP} agglomerates

Location label	Ag	Al	O	Ag:Al
AgNP-1	85.15	0.60	14.25	99.3:0.7
AgNP-2	99.5	0.5	Not detected	99.5:0.5

Table 3 Results of EDS scan using Point ID mode on specimen PM-HP-873-Ag

Location label	Ba	Co	Ag	Sb	O
Matrix	1.69	21.54	Not detected	76.78	Not detected
Ag-873-1	Not detected	1.28	73.96	24.76	Not detected
Ag-873-2	Not detected	Not detected	76.78	23.22	Not detected
Ag-873-3	Not detected	1.37	71.82	22.54	6.78

Spacing between spots is approximately 5–10 μm (Fig. 4e). Ag areas examined are 1–3 μm in diameter

Table 4 Results of EDS scan using Point ID mode on specimen PM-HP-773-Ag

Location label	Ba	Co	Ag	Sb	O
Matrix	2.14	23.96	Not detected	73.89	Not detected
Ag-773-1	Not detected	2.49	70.01	27.50	Not detected

Spacing between spots is approximately 4 μm (Fig. 4c). Ag area examined approximately 1–3 μm in diameter

Table 5 Results of EDS scan using Point ID mode on specimen PM-HP-673-Ag

Location label	Ba	Co	Ag	Sb	O
Matrix	1.44	21.01	Not detected	77.56	Not detected
Ag-673-1	Not detected	6.80	72.21	20.99	Not detected
Ag-673-2	Not detected	Not detected	92.99	7.01	Not detected
Ag-673-3	Not detected	Not detected	94.21	5.79	Not detected

Spacing between spots is approximately 5–10 μm (Fig. 4a). Ag area examined is approximately 20 μm in diameter

Although the data for the porosity dependence of elastic moduli of thermoelectric materials are relatively limited, modulus versus P data are available for $YbAl_3$ [29], LAST [55] (Table 6), and several for Co_4Sb_{12}-based skutterudites other than the Ba-filled skutterudite included in this study (Fig. 11) [49]. The b_A values for the Ba-filled skutterudite for E, G, and B in this study are bracketed by the b_A values for $YbAl_3$ and LAST for the corresponding moduli (Table 6). Also, the elastic modulus-porosity behavior for $Ba_{0.3}Co_4Sb_{12}$ in this study is quite similar to that reported by Zhang [49] for other Co_4Sb_{12}-based skutterudites (Fig. 11).

In this study, Poisson's ratio is insensitive to P for porosities $P <$ approximately 0.20, but there is considerable scatter in the data (Fig. 10d). For two previous studies of TE materials, the Poisson's ratio for LAST [55] and $YbAl_3$ [29] was essentially constant or weakly decreasing with increasing P, for P less than 0.15 or 0.12.

In this study, the scatter in Poisson's ratio (Fig. 10d) is typical of observations for porous ceramics [57, 58], and the observed relative decrease in Poisson's ratio at

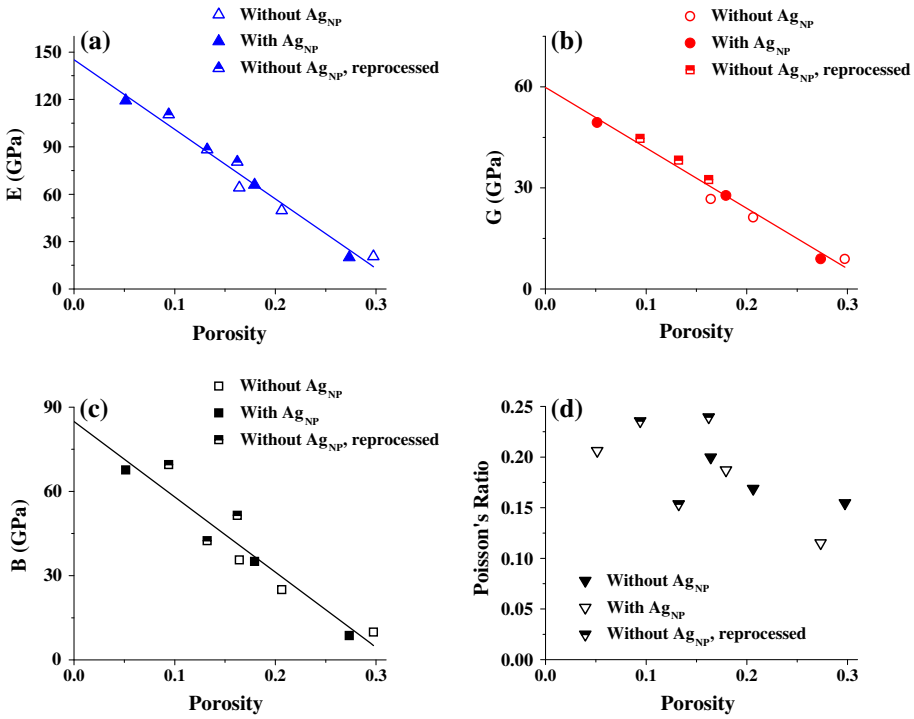

Fig. 10 The **a** Young's modulus, E, **b** shear modulus, G, and **c** bulk modulus, B, are each a function of porosity. In each figure, the solid lines represent a least-squares fit to Eq. (4b). The Poisson's ratio (**d**) is observed to be a weak function of porosity. The elastic moduli were not observed to be a function of the addition of 0.5 wt % Ag_{NP} or of reprocessing

Table 6 The linear decrease in elastic moduli, E, G, and B, according to Eq. (4b), for this study of $Ba_{0.3}Co_4Sb_{12}$ is consistent with the limited information available in the literature for porosity dependence of elastic moduli for thermoelectric materials [29, 55]

Material	A_0 (GPa)	b	N	P_{range}	R^2	Reference
$Ba_{0.3}Co_4Sb_{12}$ + 0.5 wt % Ag_{NP}, E	143 ± 4 (E_0)	3.11 ± 0.08	3	0.05–0.27	0.998	This study
$Ba_{0.3}Co_4Sb_{12}$, E	146 ± 9 (E_0)	3.00 ± 0.16	6	0.09–0.30	0.955	This study
$YbAl_3$, E	174.0 ± 2.5 (E_0)	2.34 ± 0.06	7	0.03–0.23	0.994	[29]
LAST, E	58.3 ± 0.3 (E_0)	3.6 ± 0.1	12	0.01–0.14	0.994	[55]
$Ba_{0.3}Co_4Sb_{12}$ + 0.5 wt % Ag_{NP}, G	59 ± 2 (G_0)	3.07 ± 0.08	3	0.05–0.27	0.998	This study
$Ba_{0.3}Co_4Sb_{12}$, G	60 ± 3 (G_0)	2.96 ± 0.15	6	0.09–0.30	0.962	This study
$YbAl_3$, G	73.6 ± 0.9 (G_0)	2.38 ± 0.06	7	0.03–0.23	0.995	[29]
LAST, G	22.9 ± 0.1 (G_0)	3.5 ± 0.1	12	0.01–0.14	0.991	[55]
$Ba_{0.3}Co_4Sb_{12}$ + 0.5 wt % Ag_{NP}, B	82 ± 2 (B_0)	3.25 ± 0.05	3	0.05–0.27	0.999	This study
$Ba_{0.3}Co_4Sb_{12}$, B	87 ± 10 (B_0)	3.14 ± 0.31	6	0.09–0.30	0.857	This study
$YbAl_3$, B	91.3 ± 2.9 (B_0)	2.22 ± 0.14	7	0.03–0.23	0.947	[29]

P greater than about 0.20 may be reasonably expected. Ramakrishnan and Arunachalam developed a model using 2-dimensional finite element simulation showing Poisson's ratio approaches 0.25 as porosity increases [57]. However, the model does not agree with the available data on porous ceramics [58], and may be limited by the nature of the model, ignoring the heterogeneity of porosity [59]. Furthermore, Rice argues that any model should converge to 0 for $P = 1$, and argues that Poisson's ratio should generally decrease when approaching higher values of P [59]. In an examination of both pore shape and P, Dunn and Ledbetter determine that Poisson's ratio may increase, decrease, or remain unchanged, depending on pore shape and distribution [60]. Thus, for a Poisson's ratio in the range of about 0.20 to 0.25 (for the pore-free material), the experimental observations [57–59] and theoretical predictions [57, 60] agree that Poisson's ratio is nearly independent of P (for spherical pores) over the interval from approximately $0 < P < 0.20$, which agrees with behavior observed for the Ba-skutterudites in this study (Fig. 10d).

Elastic moduli and grain size/processing effects

There was no observed difference between porosity-dependent modulus behavior of the reprocessed specimens and the HP specimens (Fig. 10). The elastic moduli of the

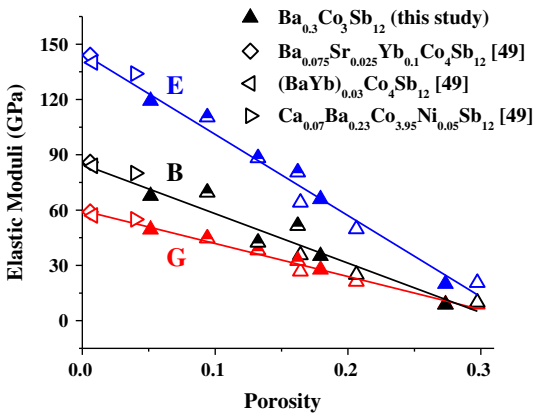

Fig. 11 The elastic moduli for the exact composition of skutterudite in this study are not recorded in literature, however the moduli for specimens of similar composition [49] are consistent with the porosity dependent elastic moduli relationships observed in this study. Filled symbols indicate specimens with 0.5 wt % Ag_{NP}, unfilled for specimens without any Ag_{NP}, and half-filled symbols for reprocessed specimens without any Ag_{NP}. The solid lines represent a least-squares fit to Eq. (4b) of the data in this study

skutterudite $Ba_{0.3}Co_4Sb_{12}$ in this study (Fig. 10) are not functions of grain size (Figs. 5, 6, 7, and 8; Table 7) or processing (Table 1). Grain size varied from bimodal with grains up to approximately 20 μm across (Figs. 5, 6; Table 7) to less than 0.2 μm (Figs. 7, 8; Table 7), based on processing by PM and HP, or reprocessed by VM and PECS (Table 1).

The bimodal grain size distribution is not expected to influence the elastic moduli of the material, as the elastic moduli of materials with grain sizes greater than approximately 20 nm are typically not a function of grain size [61]. The distribution of porosity may be influenced by the microstructure, with associated influences on elastic moduli; however, previous studies of TE materials showed only a relation based on the volume fraction porosity and no pore distribution or shape factor required to describe the modulus–porosity relationship [29, 55].

Hardness and fracture toughness results

Specimens PM-HP-673 and PM-HP-673-Ag, both hot pressed at 673 K, were too fragile to polish, limiting the hardness and fracture toughness measurements for the HP specimens to the two sintered at 773 K and the two sintered at 873 K. However, H and K_C measurements were made on each of the three reprocessed PECS specimens since all of those specimens had sufficient mechanical integrity so that polishing and indentation were not a problem. Also, for the toughness measurements, radial cracks were not present at a Vickers indentation load of 1.96 N for any of the specimens except VM-PECS-673 and VM-PECS-773, nor at 2.94 N for specimen PM-HP-673, so no K_C data are reported for the 1.96 N indentations for any specimen, nor at 2.94 N for specimen PM-HP-673 (Fig. 12).

Hardness and toughness as a function of Ag addition

As was the case for the elastic moduli, the hardness and fracture toughness of the Ba-skutterudite in this study were not sensitive to the Ag_{NP} addition (Fig. 12; Table 7). For H, much of the literature on micro-sized and nanosized metallic particles added to brittle matrices has focused on higher volume percentages. For example, H of alumina decreased from 18 GPa to 9.5 GPa with the addition of 0.20 volume fraction aluminum particles (average XRD crystallite size of 25 nm, TEM grain size 26 ± 3 nm) [62], and from 8.2 GPa to 7.3 GPa in hydroxyapatite with the addition of 5 wt % irregularly shaped 67 %Ti–33 %Fe particles which were less than 200 μm across [63].

However, the choice of Pt_{NP} or Ag_{NP} additions strongly effected the observed change in the hardness and fracture toughness of porcelain. The H and K_C were 4.94 ± 0.33 GPa and 1.36 ± 0.03 MPa·m^{½}, respectively, for the porcelain matrix itself. The addition of Ag_{NP} raised the H and K_C to 6.10 ± 0.14 GPa and 1.54 ± 0.05 MPa·m^{½}, 23 and 13 % greater, respectively, than the H and K_C of the matrix. In contrast, after the addition of 26 wt % Pt_{NP}, the hardness and fracture toughness were essentially unchanged from that of the dental porcelain matrix with $H = 5.05 \pm 0.15$ GPa and $K_C = 1.42 \pm 0.02$ MPa·m^{½}. Thus, while the addition of Pt_{NP} left both the H and K_C values essentially intact, the addition of an equivalent weight % of Ag_{NP} to the same porcelain matrix material resulted in large changes in both H and K_C [64]. For dilute concentrations of nanoparticles, changes in the elastic modulus are typically on the order of a few percent or less.

Hardness and fracture toughness as function of porosity

Hardness as function of porosity In this study, the hardness, H, of $Ba_{0.3}Co_4Sb_{12}$ and $Ba_{0.3}Co_4Sb_{12}$–Ag_{NP} decreased linearly with increasing porosity (Fig. 12a). In general, hardness is a function of porosity for ceramics or brittle semiconductors [65–67]. A least-squares fit of the H versus volume fraction porosity, P, data was done to the relationship

$$H = H_0(1 - b_H P) \quad (5)$$

where H_0 = the value of hardness at $P = 0$ and b_H is a unitless constant that describes the rate of decrease in H with increasing P. For the four HP specimens, a least-squares fit of the hardness-porosity data to Eq. (5) yielded $H_0 = 4.3 \pm 0.2$ GPa and $b_H = 3.6 \pm 0.2$ with the coefficient of determination $R^2 = 0.84$ (Fig. 12a). For the three

Table 7 For $CoSb_3$-based thermoelectric materials, a comparison of the K_C results from this study with the literature, including the porosity, P, the grain size, GS, of the specimens and the K_C measurement technique [69–71]

Material	K_C (MPam$^{0.5}$)	P	GS (μm)	K_C measurement method	Reference
$Ba_{0.3}Co_4Sb_{12}$	0.8–1.3	0.09–0.20	Bimodal [a], 0.14–0.17	Vickers indentation	This study
$Ba_{0.3}Co_4Sb_{12}$-0.5 wt % Ag	1.0–1.3	0.05–0.18	Bimodal [a]	Vickers indentation	This study
$CoSb_3$	1.7	<0.01	NA	Chevron notch bend	[69]
$CeFe_{3-x}Ru_xSb_{12}$	1.1–2.8	<0.01	NA	Chevron notch bend	[69]
$CoSb_3$	0.82 ± 0.11	Nearly dense	1–2 μm, 15 μm	Vickers indentation	[70]
$CoSb_3$	0.52 ± 0.04	Nearly dense	1–2 μm, 15 μm	Crack opening displacement	[70]
$CoSb_3$	0.51 ± 0.06	Nearly dense	15 μm	Single-edge vee-notch bend	[70]
0.1In $CoSb_3$	0.46 ± 0.13	Nearly dense	15–40 μm	Vickers indentation	[70]
0.1In $CoSb_3$	0.49 ± 0.03	Nearly dense	15–40 μm	Crack opening displacement	[70]
0.1In $CoSb_3$	0.57 ± 0.06	Nearly dense	15 μm	Single-edge vee-notch bend	[70]
Fe_4Sb_{12}- and Fe_3CoSb_{12}-based [b]	1.5 to 2.2	Typically < 0.02 [b]	NA	Vickers indentation	[71]

NA information not available

[a] Bimodal specimens had matrix grain sizes of 0.3–3 μm, with larger grains approximately 5–20 μm across

[b] $DD_{0.88}Fe_4Sb_{12}$, P = 0.014; $Ca_{0.41}DD_{0.41}Fe_4Sb_{12}$, P = 0.015; $Ba_{0.44}DD_{0.42}Fe_4Sb_{12}$, P = 0.018; $Ca_{0.20}Sr_{0.12}DD_{0.39}Fe_3CoSb_{12}$, P = 0.011; $Ca_{0.20}Ba_{0.14}DD_{0.38}Fe_3CoSb_{12}$, P not given; $Sr_{0.12}Ba_{0.18}DD_{0.39}Fe_3CoSb_{12}$, P = 0.010; $Sr_{0.066}Ba_{0.066}Yb_{0.066}Co_4Sb_{12}$, P not given; $Mm_{0.78}Fe_3CoSb_{12}$, P not given

Table 8 For spherical metallic particle additions to brittle matrices [64, 91], comparison of the measured composite modulus, E_C, with the values predicted by the four models given in this Appendix (rule of mixtures, ROM, Reuss constant strain, RCS, Hashin particulate, HP, and Halpin–Tsai, HT [90])

Material [reference]	E_m (GPa)	E_r (GPa)	V_r (%)	E_C (GPa)	ROM (GPa)	RCS (GPa)	HP (GPa)	HT (GPa)
Sodium borosilicate glass + W [91]	80.5 [91]	409.8 [92]	10	90.9 ± 1.4	113.4	87.5	92.1	96.2
Sodium borosilicate glass + W [91]	80.5 [91]	409.8 [92]	20	105.5 ± 1.1	146.4	95.9	105.5	114.1
Sodium borosilicate glass + W [91]	80.5 [91]	409.8 [92]	30	118.0 ± 0.2	179.3	106.1	121.1	134.7
Sodium borosilicate glass + W [91]	80.5 [91]	409.8 [92]	40	137.5 ± 0.3	212.2	118.6	139.6	158.7
Sodium borosilicate glass + W [91]	80.5 [91]	409.8 [92]	50	159.9 ± 0.5	245.2	134.6	161.9	186.8
Dental porcelain + Pt_{NP} [64]	60.1 [64]	177.6 [93]	11.7	67.2 ± 1.6	73.9	65.2	67.5	69.7
Dental porcelain + Ag_{NP} [64]	60.1 [64]	82 [94, 95]	21.4	67.8 ± 4.3	64.8	63.7	64.2	65.0

E_m is the Young's modulus of the matrix material [64, 91] and E_r is the Young's modulus of the reinforcing material [92–95]

reprocessed specimens, $H_0 = 6.0 \pm 0.5$ GPa and $b_H = 3.0 \pm 0.4$, with $R^2 = 0.67$ (Fig. 12a). The low R^2 is likely due to the small data set (three reprocessed specimens) and scatter in the data.

Fracture toughness as function of porosity The fracture toughness of the specimens in this study is independent of porosity, averaging 1.0 ± 0.2 MPa-m^{½} over the entire range of porosity for which K_C was measured in in this study, namely from $P = 0.05$ to 0.21 (Fig. 12b; Table 1). Note that fracture toughness was not measured for specimens PM-HP-673 ($P = 0.30$) or PM-HP-673-Ag ($P = 0.27$) since these specimens were too fragile to be polished. In the literature, it has been noted that K_C can increase, decrease, or remain unchanged with increasing P [59, 68].

In a comprehensive review of the effects of porosity on the mechanical properties of brittle materials [59], Rice noted, especially for the intermediate porosity range from roughly $P = 0.1$ to $P = 0.15$, there are a number of examples of materials in the literature (including Al_2O_3, B_4C, Si_3N_4) showing "that K_{IC} values for some of these porous bodies were clearly at least as high or higher than bodies with little or no porosity." Proposed mechanisms for an increasing or constant K_C with increasing porosity include crack–pore interactions, where pores can blunt or deflect a growing crack [18, 19].

Hardness and fracture toughness as a function of load

Over the indentation load range of 1.96 N to 9.8 N that is included in this study, both H and K_C were independent of

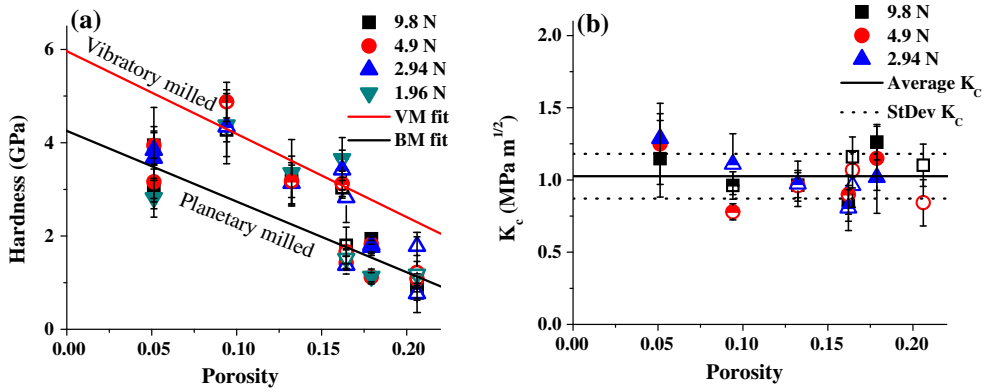

Fig. 12 The **a** hardness and **b** fracture toughness for the hot pressed specimens with Ag_{NP}, filled symbols, the hot pressed specimens without Ag_{NP}, open symbols, and the reprocessed PECS specimens without Ag_{NP}, half-filled symbols, from Vickers indentation at four loads, 9.8, 4.9, 2.94, and 1.96 N. Full radial cracks were not observed on the specimens at 1.96 N load and therefore no fracture toughness values are available at 1.96 N load. The hot pressed specimens sintered at 673 K were not able to be polished and were not tested. The *solid lines* in **a** represent hardness for the reprocessed specimens were fit to Eq. (5) separately from the hot pressed specimens because hardness is a function of grain size. Fracture toughness, **b**, was not observed to be a function of either porosity or load, as plotted by the average (*solid*) and standard deviation (*dotted*) lines, with an average K_C for all 7 specimens of 1.0 ± 0.2 MPa-m^{½}

the load for Ba-skutterudite (Fig. 12). The H, while independent of load, varied between specimens, but the K_C was essentially constant for all seven specimens examined. The average K_C of the seven specimens in this study is 1.0 ± 0.2 MPa-m^{½}, which is comparable to the K_C range of 0.46 MPa-m^{½} to 1.7 MPa-m^{½} measured for similar skutterudites (Table 7) [69–71].

For K_C, the fracture toughness should ideally be independent of load. In order to test this load independence, the $c^{3/2}$ (where c = radial crack length) versus indentation load, F, behavior was examined for each of the Ba-skutterudite specimens included in this study. A plot of $c^{3/2}$ versus F yielded a straight line plot with $R^2 > 0.98$ in each case, as demonstrated by plots from specimens VM-PECS-673 and PM-HP-873-Ag (Fig. 13). Thus, the radial crack length versus indentation load behavior is consistent with Eq. (3) for each specimen in this study, where Eq. (3) can be rewritten as

$$c^{3/2} = \frac{\xi (E/H)^{0.5} F}{K_C} \tag{6}$$

For a given specimen, we assume the ξ, E, H. and K_C are constant, thus Eq. (6) is a straight line. The high value of R^2 for the least-squares fit to Eq. (6) supports the use of Eq. (3) to calculate K_C.

In contrast to K_C, hardness is frequently observed to be a function of the applied load. From the literature, for both metals [72, 73] and brittle solids [74, 75], the measured hardness can be a function of the applied indentation load. The indentation size effect (ISE) [73], where H decreases as the applied load increases, has been ascribed to elastic recovery and working hardening during indentation [74, 75] while an observed reverse indentation size effect (RISE) [76], where H decreases with decreasing load has been attributed to stress relaxation during unloading [76].

Hardness and fracture toughness results as a function of grain size

The hardness varied as a function of grain size, as observed by the fit to Eq. (5) in Fig. 12a, while the fracture toughness is independent of grain size, averaging 1.0 ± 0.2 MPa-m^{½} (Table 7). For the bimodal grain size HP specimens (matrix grain sizes of 0.3–3 μm, with larger grains approximately 5–20 μm across), the H_0 is 4.3 ± 0.2 GPa, while for the reprocessed specimens with average grain sizes of 0.17 μm, 0.16 μm, and 0.14 μm, the H_0 is 6.0 ± 0.5 GPa (Fig. 12a).

Hardness results as a function of grain size The difference in H_0 between planetary milled and HP specimens and the vibratory milled and PECS-processed specimens likely is related to the grain size dependence of H. A Hall–Petch type relationship between H and grain size, GS, available in the literature is [77]

$$H = H_0 + kGS^{-1/2} \tag{7}$$

where H_0 is considered as the H value in the single-crystal limit and k is called the Petch parameter. While Hall–Petch behavior is very common in metals [78], the nature of the H versus GS dependence is uncertain for many ceramics [77, 79]. Hall–Petch behavior is common for relatively soft ceramics such as alkaline halides, but there is a great deal of scatter in the H versus GS data for most hard ceramics [77, 79]. Furthermore, the H_0 obtained from H versus GS data if not always a good predictor for the H of single

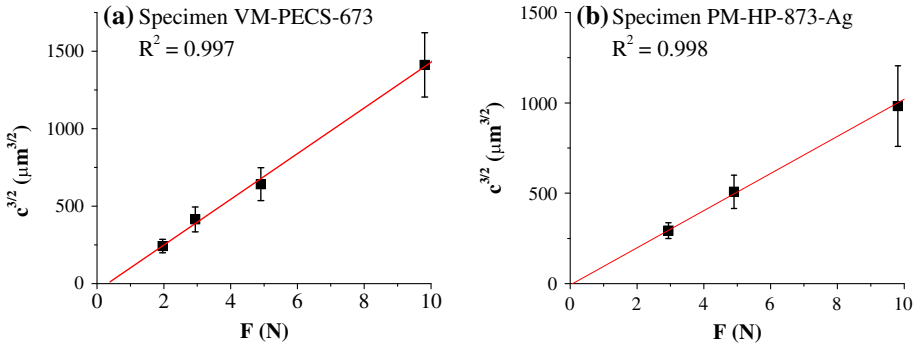

Fig. 13 For each of the specimens, a plot of $c^{3/2}$ versus load, F, was used to determine the suitability of the fracture toughness by Vickers indentation. For 5 of 7 specimens, the coefficient of determination, R^2, for a linear regression to Eq. (6) through the data points is 0.99 or greater, with an R^2 of 0.98 for specimen VM-PECS-773, and 0.84 for specimen PM-HP-773. Note specimen PM-HP-773 also has a low fracture toughness measurement at 2.94 N load. All specimens were measured at three loads, except VM-PECS-673 and VM-PECS-773 with a fourth measurement at a Vickers indentation load of 1.96 N

crystals (as is typically assumed for Eq. (7)) [77]. In addition, for some ceramics, such as ZrO_2 and $AlMg_2O_4$, H is independent of grain size [77]. Also, minima in H versus GS data are often observed for intermediate grain sizes (GS on the order of several μm) such that the Petch parameter k can take on both negative and positive values (with unequal magnitudes) for a given data set [77, 79]. Nevertheless, a well-accepted alternative to Eq. (7) is not available in the literature and thus, in general, the H versus GS behavior for brittle materials is not clear from the standpoint of the available data or the available functional relationship (Eq. (7)).

Fracture toughness results as a function of grain size In this study, fracture toughness, K_C, is essentially independent of grain size, GS, averaging 1.0 ± 0.2 MPa-m$^{1/2}$ (Fig. 12b).

This result may be counterintuitive, since fracture strength is typically a function of grain size [33]. However, fracture strength is based on the stress required for failure of a specimen and is typically dependent on the largest flaw, and the intrinsic flaw size typically scales with GS [33]. In contrast, K_C is based on the work necessary to extend a crack [33], which may or may not be related to grain size.

Thus, grain size engineering alone will not likely improve fracture toughness either for Ba-skutterudite or other cubic thermoelectric materials. Although no studies are currently available in the literature for the grain size dependence of K_C for thermoelectric materials, K_C has been observed to be essentially independent of grain size for various cubic materials, tested using a variety of test methods, including Y_2O_3 (notched beam test [80] and double cantilever beam technique [81]), MgO (Chevron notch method [82]), NiZn ferrite (notched beam [83]), and $MgAl_2O_4$ (double cantilever bean and Vickers indentation [84]). In addition, for noncubic materials with small grain size, K_C can be independent of grain size as was the case in a study by Yao et al. who found that K_C was independent of grain size for PECS-processed, fully dense polycrystalline alumina with grain sizes ranging from 0.3 to 3.3 μm for K_C measured by the surface crack in flexure technique [85].

In contrast to cubic materials, for noncubic materials with intermediate grain sizes (roughly on the order of 10–100 μm), a maximum in K_C has been observed as a function of grain size [6]. Lawn and co-workers ascribed the observed increase in K_C with increasing grain size to grain bridging [86–88], with the principle mechanism responsible for grain bridging being the clamping forces generated by thermal expansion anisotropy [89]. After the maximum in K_C, K_{CMAX}, is reached, the subsequent decrease in K_C with further increases in grain size has been linked to thermal expansion anisotropy-induced microcracking in noncubic materials, where the grain size at K_{CMAX} coincides roughly with the critical grain size for microcracking [56]. Thus, while for noncubic materials, a grain-size-dependent maximum in K_C has been observed, the insensitivity of K_C to grain size for the cubic Ba-skutterudite in this study is consistent with the literature. In addition to the grain size and porosity trends, the value of K_C for the Ba-skutterudite measured in this study is comparable to K_C values in the literature for other $CoSb_3$ systems [69–71] (Table 7).

Summary and conclusions

In this study, the elastic moduli (Fig. 10), hardness (Fig. 12a), and fracture toughness (Fig. 12b) of $Ba_{0.3}Co_4Sb_{12}$ were insensitive to the addition of 0.5 wt % Ag_{NP}. Both the elastic moduli and hardness were functions of porosity (Figs. 10, 12a), which agrees with previous

literature results for elasticity (Fig. 11) [49] and hardness [65–67]. Fracture toughness (Fig. 12b) was not a function of porosity (Fig. 12b), which may indicate an interaction between the pores and the growing cracks.

The study by Zhou [8] demonstrated that Ag addition results in important changes in thermoelectric properties (increasing electrical conduction) for Ba-skutterudite. However, this study indicates that the addition of silver also affects the densification process which in turn can affect changes in mechanical properties. At a sintering temperature of 873 K, the specimen without Ag_{NP} had a P value of 0.16 while the specimen sintered with 0.5 wt % Ag_{NP} had $P = 0.05$. The increased densification with the addition of Ag was likely due to a liquid-phase sintering from the pertitectic reaction that formed the Ag_3Sb phase observed in the specimen.

Based on the results of this study, a similar peritectic reaction may explain the formation of Ag_3Sb and an enhanced ZT when Ag was added to ZnSb [50]. Similar peritectic or eutectic reactions may take place in other antimonide thermoelectric systems when Ag or another conductive material is added to enhance electrical conductivity. More generally, this type of eutectic or peritectic reaction to enhance densification and improve electrical conductivity may operate in a number of thermoelectric systems in addition to antimonides. Although a set of ternary or quaternary phase diagrams may not be available for many thermoelectric systems, a search of binary-phase diagrams (such as the Ag–Sb phase diagrams used in this study) may act as a guide to discover potential beneficial peritectic or eutectic reactions.

Acknowledgements The authors acknowledge the financial support of the Department of Energy, Revolutionary Materials for Solid State Energy Conversion Center, an Energy Frontiers Research Center funded by the U.S. Department of Energy, Office of Science, Office of Basic Energy Sciences under award number DE-SC0001054.

Appendix A: Effect of nanoparticle addition on the elastic modulus of a composite material

The effect of the nanoparticle additions on the Young's modulus, E_C, of a nanocomposites material can be predicted from numerous models. In this Appendix, we list relationships for four composite models, namely rule of mixtures (ROM), Reuss constant strain (RCS), Hashin particulate (HP), and Halpin–Tsai (HT) [90]. For each model, the Young's modulus of the composite, E_C, is the based on E_r, the elastic modulus of the nanoparticle reinforcement phase, V_r, the volume fraction reinforcement phase, E_m, the Young's modulus of the matrix phase, and, V_m, the volume fraction matrix phase. Expressions for the four models can be written as

$$\text{ROM} : E_C = V_m E_m + V_r E_r \tag{8}$$

$$\text{RCS} : \frac{1}{E_C} = \frac{V_m}{E_m} + \frac{V_r}{E_r} \tag{9}$$

$$\text{HP} : E_C = E_m \left(\frac{E_m V_m + E_r\{V_f + 1\}}{E_r V_m + E_m\{V_r + 1\}} \right) \tag{10}$$

$$\text{HT} : E_C = E_m \left(\frac{1 + 2(a/b) q V_r}{E_r V_m + E_m\{V_r + 1\}} \right) \tag{11}$$

In the HT model, a/b is the aspect ratio (length/thickness) for the reinforcing phase and q is a boundary condition parameter given by

$$q = \frac{\left(\frac{E_r}{E_m}\right) - 1}{\left(\frac{E_r}{E_m}\right) + 2\left(\frac{a}{b}\right)} \tag{12}$$

Table 8 summarizes the Young's modulus change due to the addition of both micron-sized and nanosized-metallic particles to brittle matrices in studies by Hasselman [91] and by Fujieda et al. [64]. Table 8 gives the measured composite modulus, E_C, for the addition of 0.10, 0.20, 0.30, and 0.40 volume fraction of tungsten particles with diameters of approximately 30 μm to a borosilicate glass [91], along with the predicted values of modulus calculated by the ROM, RCS, HP, HT models and the modulus of tungsten [92]. In addition, Table 8 lists the measured E_C, for composite specimens from Fujieda et al. [64], who measured the elastic modulus change induced by adding either 26 wt % platinum nanoparticles (Pt_{NP}) [93] or 26 wt % Ag_{NP} [94, 95] to a dental porcelain, where the mean diameters of the Pt_{NP} and Ag_{NP} nanoparticles were 5 nm and 10 nm, respectively. The measured composite moduli, E_C, (Table 8) [64, 91] agree quite well with the moduli calculated in this study using the Halpin–Tsai model (HT). Since the metal particles were spherical in both the Hasselman [91] and Fujieda et al. [64] studies, for the purposes of the calculations, we set $a/b = 1$ in Eq. (11), where a/b is the particle aspect ratio.

The amounts of particle addition in the studies by Fujieda et al. [64] and Hasselman [91] were significantly greater than the 0.0068 volume fraction (0.5 wt %) Ag_{NP} added in this study. The four composite models given in this Appendix predict a decrease in E_C of about 0.39 % with the 0.5 wt % Ag_{NP} addition to the Ba-skutterudite in this study. In recent research by Schmidt et al. [90] applied the four modulus-composite models to a thermoelectric system consisting of a brittle matrix and a brittle reinforcing phase, namely with 0.00, 0.01, 0.02, 0.03, and 0.04 volume fraction of added SiC nanoparticles (SiC_{NP}) in the brittle thermoelectric matrix $SnTe_{1+X}$, (where $x = 0.0$ or 0.016), Hashin and the Halpin–Tsai models best described the elastic modulus data. Thus, for the Hasselman [91] and

Fujieda et al. [64] studies in which the volume percentage of micro- and nano-particles added was relatively high (from 0.10 to 0.40 volume fraction), as well as the $SnTe_{1+X}$ (with 0.00 to 0.04 volume fraction SiC_{NP} added), the Haplin–Tsai model agrees with the experimental modulus data relatively well. In particular, for 0.5 wt % Ag_{NP} in this study, the Haplin–Tsai model predicts a change in E of only 0.35 %, which is consistent with the E values measured in this study for the Ba-skutterudite with and without added Ag_{NP}.

References

1. Ioffe AF (1960) Physics of semicondutors. Infosearch Limited, London, p 313
2. Shi X, Yang J, Salvador JR, Chi M, Cho JY, Wang H, Bai S, Yang J, Zhang W, Chen L (2011) Multiple-filled skutterudites: high thermoelectric figure of merit through separately optimizing electrical and thermal transports. J Am Chem Soc 133:7837–7846
3. Segerlind LG (1984) Applied finite element analysis, 2nd edn. Wiley, New York
4. Hutton D (2004) Fundamentals of finite element analysis. McGraw-Hill, Boston
5. Zienkiewicz OC, Taylor RL (2005) The finite element method for solid and structural mechanics, 6th edn. Elsevier Butterworth-Heinemann, Boston
6. Wachtman JB, Cannon WR, Matthewson MJ (2009) Mechanical properties of ceramics. Wiley-VCH, Hoboken
7. Ren F, Case ED, Timm EJ, Schock HJ (2008) Hardness as a function of composition for *n*-type LAST thermoelectric material. J Alloy Compd 455:340–345
8. Zhou X, Wang G, Zhang L, Chi H, Su X, Sakamoto J, Uher C (2012) Enhanced thermoelectric properties of Ba-filled skutterudites by grain size reduction and Ag nanoparticle inclusion. J Mater Chem 22:2958–2964
9. Androulakis J, Lin C-H, Kong H-J, Uher C, Wu C-I, Hogan T, Cook BA, Caillat T, Paraskevopoulos KM, Kanatzidis MG (2007) Spinodal decomposition and nucleation and growth as a means to bulk nanostructured thermoelectrics: enhanced performance in Pb(1 − x)Sn(x)Te-PbS. J Am Chem Soc 129:9780–9788
10. Zhao LD, He J, Hao S, Wu C-I, Hogan TP, Wolverton C, Dravid VP, Kanatzidis MG (2012) Raising the thermoelectric performance of *p*-type PbS with endotaxial nanostructuring and valence-band offset engineering using CdS and ZnS. J Am Chem Soc 134:16327–16336
11. Zhou M, Li J-F, Kita T (2008) Nanostructured AgPb(m)Sb-Te(m + 2) system bulk materials with enhanced thermoelectric performance. J Am Chem Soc 130:4527–4532
12. Alleno E, Chen L, Chubilleau C, Lenoir B, Rouleau O, Trichet MF, Villeroy B (2009) Thermal conductivity reduction in $CoSb_3$–CeO_2 nanocomposites. J Electron Mater 39:1966–1970
13. Ji X, He J, Alboni P, Su Z, Gothard N, Zhang B, Tritt TM, Kolis JW (2007) Thermal conductivity of $CoSb_3$ nano-composites grown via a novel solvothermal nano-plating technique. Phys Status Solidi RRL 1:229–231
14. Toprak MS, Stiewe C, Platzek D, Williams S, Bertini L, Muller E, Gatti C, Zhang Y, Rowe M, Muhammed M (2004) The impact of nanostructuring on the thermal conductivity of thermoelectric $CoSb_3$. Adv Funct Mater 14:1189–1196
15. Mi JL, Zhao XB, Zhu TJ, Tu JP (2008) Thermoelectric properties of Yb 0.15 Co 4 Sb 12 based nanocomposites with CoSb 3 nano-inclusion. J Phys D 41:205403
16. Yoon S, Kwon O-J, Ahn S, Kim J-Y, Koo H, Bae S-H, Cho J-Y, Kim J-S, Park C (2013) The effect of grain size and density on the thermoelectric properties of Bi_2Te_3–PbTe compounds. J Electron Mater 42:3390–3396
17. Tokiai T, Uesugi T, Nosaka M, Hirayama A, Ito K, Koumoto K (1997) Thermoelectric properties of Mn-doped iron disilicide ceramics fabricated from radio-frequency plasma-treated fine powders. J Mater Sci 32:3007–3011. doi:10.1023/A:1018609508637
18. Case ED (2012) Thermal fatigue and waste heat recovery via thermoelectrics. J Electron Mater 41:1811–1819
19. Case ED (2012) Chapter 16, Thermo-mechanical properties of thermoelectric materials. In: Rowe DM (ed) Thermoelectrics and its energy harvesting: modules, systems and applications. CRC Press, Taylor and Francis Group, Boca Raton, pp 16-1 to 16-29
20. Lee H, Vashaee D, Wang DZ, Dresselhaus MS, Ren ZF, Chen G (2010) Effects of nanoscale porosity on thermoelectric properties of SiGe. J Appl Phys 107:094308
21. Yang L, Wu JS, Zhang LT (2004) Synthesis of filled skutterudite compound $La_{0.75}Fe_3CoSb_{12}$ by spark plasma sintering and effect of porosity on thermoelectric properties. J Alloy Compd 364:83–88
22. He Q, Hu S, Tang X, Lan Y, Yang J, Wang X, Ren Z, Hao Q, Chen G (2008) The great improvement effect of pores on ZT in $Co_{1-x}Ni_xSb_3$ system. Appl Phys Lett 93:042108
23. Wen P, Duan B, Zhai P, Li P, Zhang Q (2013) Effect of thermal annealing on the microstructure and thermoelectric properties of nano-TiN–$Co_4Sb_{11.5}Te_{0.5}$ composites. J Mater Sci: Mater Electron 24:5155–5161
24. Pilchak AL, Ren F, Case ED, Timm EJ, Schock HJ, Wu C-I, Hogan TP (2007) Characterization of dry milled powders of LAST (lead–antimony–silver–tellurium) thermoelectric material. Philos Mag 87:4567–4591
25. Ren F, Case ED, Ni JE, Timm EJ, Lara-Curzio E, Trejo RM, Lin C-H, Kanatzidis MG (2009) Temperature-dependent elastic moduli of lead telluride-based thermoelectric materials. Philos Mag 89:143–167
26. Ni JE, Case ED, Khabir KN, Stewart RC, Wu C-I, Hogan TP, Timm EJ, Girard SN, Kanatzidis MG (2010) Room temperature Young's modulus, shear modulus, Poisson's ratio and hardness of PbTe–PbS thermoelectric materials. Mater Sci Eng B 170:58–66
27. Schmidt RD, Ni JE, Case ED, Sakamoto JS, Kleinow DC, Wing BL, Stewart RC, Timm EJ (2010) Room temperature Young's modulus, shear modulus, and Poisson's ratio of $Ce_{0.9}Fe_{3.5}Co_{0.5}Sb_{12}$ and $Co_{0.95}Pd_{0.05}Te_{0.05}Sb_3$ skutterudite materials. J Alloy Compd 504:303–309
28. Migliori A, Sarrao JL (1997) Resonant ultrasound spectroscopy: applications to physics, materials measurements, and nondestructive evaluation. Wiley-VCH, New York
29. Schmidt RD, Case ED, Lehr GJ, Morelli DT (2013) Room temperature mechanical properties of polycrystalline $YbAl_3$, a promising low temperature thermoelectric material. Intermetallics 35:15–24
30. Lawn BR, Cook RF (2012) Probing material properties with sharp indenters: a retrospective. J Mater Sci 47:1–22. doi:10.1007/s10853-011-5865-1
31. Underwood EE (1969) Stereology, or the quantitative evaluation of microstructures. J Microsc 89:161–180
32. Case ED, Smyth JR, Monthei V (1981) Grain-size determinations. J Am Ceram Soc 64:C24–C25
33. Barsoum MW (2003) Fundamentals of ceramics. Taylor & Francis Group, New York

34. Voronin MV, Osadchii EG (2013) Standard thermodynamic properties of Ag_3Sb and Ag_6Sb evaluated by EMF measurements. Inorg Mater 49:550–554
35. Cipriani C, Corazza M, Mazzetti G (1996) Reinvestigation of natural silver antimonides. Eur J Mineral 8:1347–1350
36. Feschotte P, Monachon F, Durussel P (1992) The binary system Sb–Ag: a revision of the Ag_3Sb phase boundaries. J Alloy Compd 186:L17–L18
37. Okamoto H (2007) Ag–Sb (silver–antimony). J Phase Equilibria 28:403
38. Hassam S, Bahari Z, Legendre B (2001) Phase diagrams of the Ag–Bi–Sb ternary system. J Alloy Compd 315:211–217
39. Okamoto H (1993) Ag–Sb (silver–antimony). J Phase Equilibria 14:531–532
40. Zhang L, Sakamoto J (2013) The microstructural stability and thermoelectric properties of $Mm_{0.9}Fe_{3.5}Co_{0.5}Sb_{12}$-based skutterudites. Mater Chem Phys 138:601–607
41. Bukat K, Koscielski M, Sitek J, Jakubowska M, Miozniak A (2011) Silver nanoparticles effect on the wettability of Sn–Ag–Cu solder pastes and solder joints microstructure on copper. Solder Surf Mt Technol 23:150–160
42. Dharma IGBB, Shukor MHA, Ariga T (2009) Wettability of low silver content lead-free solder alloy. Mater Trans 50:1135–1138
43. Yoshizawa M, Nakanishi Y, Kumagai T, Oikawa M, Sekine C, Shirotani I (2004) Elastic anomalies of polycrystalline $SmRu_4P_{12}$ associated with metal-insulator transition. J Phys Soc Jpn 73:315–318
44. Slack GA, Tsoukala VG (1994) Some properties of semiconducting $IrSb_3$. J Appl Phys 76:1665–1671
45. Morelli DT, Meisner GP (1995) Low temperature properties of the filled skutterudite $CeFe_4Sb_{12}$. J Appl Phys 77:3777–3781
46. Nolas GS, Morelli DT, Tritt TM (1999) Skutterudites: a phonon-glass-electron crystal approach to advanced thermoelectric energy conversion applications. Annu Rev Mater Sci 29:89–116
47. Nolas GS, Kaeser M, Littleton RT, Tritt TM (2000) High figure of merit in partially filled ytterbium skutterudite materials. Appl Phys Lett 77:1855–1857
48. Uher C (2001) Skutterudites: prospective novel thermoelectrics. In: Tritt TM (ed) Semiconductors and semimetals, vol 69. Academic Press, San Diego, pp 139–253
49. Zhang L, Rogl G, Grytsiv A, Puchegger S, Koppensteiner J, Spieckermann F, Kabelka H, Reinecker M, Rogl P, Schranz W, Zehetbauer M, Carpenter MA (2010) Mechanical properties of filled antimonide skutterudites. Mater Sci Eng B 170:26–31
50. Xiong DB, Okamoto NL, Inui H (2013) Enhanced thermoelectric figure of merit in *p*-type Ag-doped ZnSb nanostructured with Ag_3Sb. Scr Mater 69:397–400
51. Hashin Z (1962) The elastic moduli of heterogeneous materials. J Appl Mech 29:143–150
52. Halpin JC (1992) Primer on composite materials analysis. Technomic Publishing Company Inc., Lancaster
53. Bedolla E, Lemus-Ruiz J, Contreras A (2012) Synthesis and characterization of Mg–AZ91/AlN composites. Mater Des 38:91–98
54. Couturier R, Ducret D, Merle P, Disson JP, Joubert P (1997) Elaboration and characterization of a metal matrix composite: Al/AlN. J Eur Ceram Soc 17:1861–1866
55. Ni JE, Ren F, Case ED, Timm EJ (2009) Porosity dependence of elastic moduli in LAST (lead–antimony–silver–tellurium) thermoelectric materials. Mater Chem Phys 118:459–466
56. Rice RW (1998) Porosity of ceramics. Marcel Dekker, New York
57. Ramakrishan N, Arunachalam VS (1993) Effective elastic moduli of porous ceramic materials. J Am Ceram Soc 76:2745–2752
58. Boccaccini AR (1994) Comment on "Effective Elastic Moduli of Porous Ceramic Materials". J Am Ceram Soc 77:2779–2781
59. Rice RW (1995) Comment on 'Effective Elastic Moduli of Porous Ceramic Materials". J Am Ceram Soc 78:1711
60. Dunn ML, Ledbetter H (1995) Poisson's ratio of porous and microcracked solids: theory and application to oxide superconductors. J Mater Res 10:2715–2722
61. Kim HS, Bush MB (1999) The effects of grain size and porosity on the elastic modulus of nanocrystalline materials. Nanostructured Mater 11:361–367
62. Zawrah MF, Abdel-kader H, Elbaly NE (2012) Fabrication of Al_2O_3–20vol% Al nanocomposite powders using high energy milling and their sinterability. Mater Res Bull 47:655–661
63. Chang Q, Chen DL, Ru HQ, Yue XY, Yu L, Zhang CP (2010) Toughening mechanisms in iron-containing hydroxyapatite/titanium composites. Biomaterials 31:1493–1501
64. Fujieda T, Uno M, Ishigami H, Kurachi M, Wakamatsu N, Doi Y (2012) Addition of platinum and silver nanoparticles to toughen dental porcelain. Dent Mater J 31:711–716
65. Fan X, Case ED, Yang Q, Nicholas JD (2013) Room temperature hardness of gadolinia-doped ceria as a function of porosity. J Mater Sci 48:6977–6985. doi:10.1007/s10853-013-7506-3
66. Ramadass N, Mohan S, Reddy SR (1983) Studies on the metastable phase retention and hardness in zirconia ceramics. Mater Sci Eng 60:65–72
67. Mangalaraja RV, Ananthakumar S, Uma K, Jiménez RM, López M, Camurri CP (2009) Microhardness and fracture toughness of $Ce_{0.9}Gd_{0.1}O_{1.95}$ for manufacturing solid oxide electrolytes. Mater Sci Eng A 517:91–96
68. Shao Y, Du R, Wu X, Song F, Xu X, Jiang C (2013) Effect of porosity on the crack pattern and residual strength of ceramics after quenching. J Mater Sci 48:6431–6436. doi:10.1007/s10853-013-7444-0
69. Ravi V, Firdosy S, Caillat T, Lerch B, Calamino A, Pawlik R, Nathal M, Sechrist A, Buchhalter J, Nutt S (2008) Mechanical properties of thermoelectric skutterudites. Proc Am Inst Phys Conf, Space Technol Appl Int Forum, Albuquerque, NM, pp 10–14
70. Eilertsen J, Subramanian MA, Kruzic JJ (2013) Fracture toughness of Co_4Sb_{12} and $In_{0.1}Co_4Sb_{12}$ thermoelectric skutterudites evaluated by three methods. J Alloy Compd 552:492–498
71. Rogl G, Rogl P (2011) Mechanical properties of skutterudites. Sci Adv Mater 3:517–538
72. Pharr GM, Herbert EG, Gao Y (2010) The indentation size effect: a critical examination of experimental observations and mechanistic interpretations. Annu Rev Mater Res 40:271–292
73. Nix WD, Gao H (1998) Indentation size effects in crystalline materials: a law for strain gradient plasticity. J Mech Phys Solids 46:411–425
74. Bull SJ, Page TF, Yoffe EH (1989) An explanation of the indentation size effect in ceramics. Philos Mag Lett 59:281–288
75. Sangwal K (2009) Review: indentation size effect, indentation cracks and microhardness measurement of brittle crystalline solids—some basic concepts and trends. Cryst Res Technol 44:1019–1037
76. Sangwal K (2000) On the reverse indentation size effect and microhardness measurement of solids. Mater Chem Phys 63:145–152
77. Rice RW (2000) Mechanical properties of ceramics and composites. Marcel Dekker, New York
78. Lawn BR (1993) Fracture of brittle solids, 2nd edn. Cambridge University Press, New York
79. Armstrong RW (2011) The hardness and strength properties of WC–Co composites. Matereials 4:1287–1308
80. Monroe LD, Smyth JR (1978) Grain size dependence of the fracture energy of Y_2O_3. J Am Ceram Soc 61:538–539
81. Rhoades WH, Baldoni JG, Wei GC (1986) Final report for ORN contract N00014-82-C-0452. GTE Laboratory

82. Yasuda K, Kim SD, Kanemichi Y (1990) Influence of grain size and temperature on fracture toughness of MgO sintered body. J Ceram Soc Jpn 98:1103–1108
83. Veldkamp JDB, Hattu N (1979) On the fracture toughness of brittle materials. Philips J Res 34:1–25
84. Rice RW (1996) Grain size and porosity dependence of ceramic fracture energy and toughness at 22°C. J Mater Sci 31:1969–1983. doi:10.1007/BF00356616
85. Yao W, Liu J, Holland TB, Huang L, Xiong Y, Schoenung JM, Mukherjee AK (2011) Grain size dependence of fracture toughness for fine grained alumina. Scr Mater 65:143–146
86. Vekinis G, Ashby MF, Beaumont PWR (1990) R-curve behavior of Al_2O_3 ceramics. Acta Metall Mater 38:1151–1162
87. Swanson PL, Fairbanks CJ, Lawn BR, Mai YW, Hockey BJ (1987) Crack-interface grain bridging as a fracture-resistance mechanism in ceramics. J Am Ceram Soc 70:279–289
88. Foulk JW III, Cannon RM, Johnson GC, Klein PA, Ritchie RO (2007) A micromechanical basis for partitioning the evolution of grain bridging in brittle materials. J Mech Phys Solids 55:719–743
89. Bennison SJ, Lawn BR (1989) Role of interfacial grain-bridging sliding friction in the crack resistance and strength of nontransforming ceramics. Acta Metall 37:2659–2671
90. Schmidt RD, Case ED, Ni JE, Trejo RM, Lara-Curzio E, Korkosz RJ, Kanatzidis MG (2013) High-temperature elastic moduli of thermoelectric $SnTe_{1\pm x}$–ySiC nanoparticulate composites. J Mater Sci 48:8244–8258. doi:10.1007/s10853-013-7637-6
91. Hasselman DPH, Fulrath RM (1965) Effect of spherical tungsten dispersions on young's modulus of a glass. J Am Ceram Soc 48:548–549
92. Lowrie R, Gonas AM (1967) Single crystal elastic properties of tungsten from 24° to 1800°C. J Appl Phys 38:4505–4509
93. Macfarlane RE, Rayne JA (1965) Anomalous temperature dependence of shear modulus c44 for platinum. Phys Lett 18:91–92
94. Neighbours J, Alers G (1958) Elastic constants of silver and gold. Phys Rev 885:707–712
95. Chang YA, Himmel L (1966) Temperature dependence of the elastic constants of Cu, Ag, and Au above room temperature. J Appl Phys 37:3567–3572